Article

Structural and mechanistic insights into fungal β-1,3-glucan synthase FKS1

https://doi.org/10.1038/s41586-023-05856-5

Received: 29 March 2022

Accepted: 16 February 2023

Published online: 22 March 2023

Check for updates

Xinlin Hu[1,2,6], Ping Yang[1,6], Changdong Chai[1], Jia Liu[1,2], Huanhuan Sun[1], Yanan Wu[1], Mingjie Zhang[3,4], Min Zhang[1,2]✉, Xiaotian Liu[3]✉ & Hongjun Yu[1,5]✉

The membrane-integrated synthase FKS is involved in the biosynthesis of β-1, 3-glucan, the core component of the fungal cell wall[1,2]. FKS is the target of widely prescribed antifungal drugs, including echinocandin and ibrexafungerp[3,4]. Unfortunately, the mechanism of action of FKS remains enigmatic and this has hampered development of more effective medicines targeting the enzyme. Here we present the cryo-electron microscopy structures of *Saccharomyces cerevisiae* FKS1 and the echinocandin-resistant mutant FKS1(S643P). These structures reveal the active site of the enzyme at the membrane–cytoplasm interface and a glucan translocation path spanning the membrane bilayer. Multiple bound lipids and notable membrane distortions are observed in the FKS1 structures, suggesting active FKS1–membrane interactions. Echinocandin-resistant mutations are clustered at a region near TM5–6 and TM8 of FKS1. The structure of FKS1(S643P) reveals altered lipid arrangements in this region, suggesting a drug-resistant mechanism of the mutant enzyme. The structures, the catalytic mechanism and the molecular insights into drug-resistant mutations of FKS1 revealed in this study advance the mechanistic understanding of fungal β-1,3-glucan biosynthesis and establish a foundation for developing new antifungal drugs by targeting FKS.

Invasive fungal infections cause over 1.5 million death annually, posing a serious threat to public health[5]. Such infections are of substantial concern (for example, causing high mortality) for immunocompromised populations as well as patients with COVID-19 (refs. [5,6]) (https://www.cdc.gov/fungal/covid-fungal.html). Limited classes of antifungal drugs and emerging drug-resistant strains such as the recent outbreak of multidrug-resistant *Candida auris* have caused serious challenges in treating patients who are infected[7,8]. Therefore, there are pressing needs to develop new antifungal agents[8].

β-1,3-Glucan is a fundamental component of the fungal cell wall[2], thus targeting its biosynthesis is an important strategy for developing broad-spectrum antifungal drugs[3,9]. β-1,3-Glucan of the fungal cell wall is synthesized by membrane-integrated synthase FKS[10,11], which is regulated by GTPase Rho1 (refs. [12,13]). FKS transfers glucose from donor UDP-glucose to the growing chain of glucan via β-1,3-glycosidic linkages and translocates the polymerized β-1,3-glucan into the extracellular space (Fig. 1a). FKS orthologues have been identified in all analysed fungi and are essential for the viability of many prominent fungal pathogens. In *Candida glabrata* and *S. cerevisiae*, simultaneous disruption of *FKS1* and *FKS2* showed lethal phenotype[14,15]; *FKS1* of *Candida albicans* and *Cryptococcus neoformans* are essential for viability[16,17]; the mould *Aspergillus fumigatus* with an *FKS1* deletion suffers from severe growth defects and cell lysis[18]. Currently, there are two well-known antifungal drugs on the market that target FKS: echinocandin, the first-line antifungal drug widely used in clinical practice[19], and ibrexafungerp, a newly approved oral fungicidal drug[4]. More novel agents targeting FKS function (for example, rezafungin) are entering into late-stage clinical trials[4]. Unfortunately, FKS mutations are closely linked to echinocandin resistance and therapeutic failure, an emerging concern in invasive fungal infections[20,21]. Numerous clinically identified echinocandin-resistant mutations are concentrated at three conserved regions of FKS[20,22]. Mutations in a single *FKS* allele are sufficient to render fungal strains resistant to echinocandin[23].

The lack of a FKS structure has hindered our understanding of the catalytic mechanism of FKS and hampered developments of new antifungal drugs. FKS is an approximately 200-kDa membrane-embedded protein with low-sequence homologies to other characterized glycosyltransferases (GTs). FKS belongs to the GT48 family with no structures available for any of its members. Here we report the cryo-electron microscopy (cryo-EM) structures of *S. cerevisiae* FKS1 and its drug-resistant mutant FKS1(S643P). Further structure-guided functional characterizations enable us to elucidate the molecular basis of β-1,3-glucan biosynthesis by FKS1 and to rationalize drug-resistant mutations of the enzyme.

Functional characterization of FKS1

For in vivo functional studies, we combined genetic deletion of *FKS1* with pharmacological manipulation of FKS2 to circumvent the lethal phenotype caused by simultaneous disruption of both FKS1 and FKS2 in *S. cerevisiae*[15]. The wild-type (WT) strain showed modestly slowed

[1]Department of Biochemistry and Molecular Biology, School of Basic Medicine, Tongji Medical College, Huazhong University of Science and Technology, Wuhan, China. [2]Department of Pathogen Biology, School of Basic Medicine, Tongji Medical College, Huazhong University of Science and Technology, Wuhan, China. [3]School of Life Sciences, Southern University of Science and Technology, Shenzhen, China. [4]Greater Bay Biomedical Innocenter, Shenzhen Bay Laboratory, Shenzhen, China. [5]Cell Architecture Research Center, Huazhong University of Science and Technology, Wuhan, China. [6]These authors contributed equally: Xinlin Hu, Ping Yang. ✉e-mail: minzhang@hust.edu.cn; liuxt@sustech.edu.cn; hongjun_yu@hust.edu.cn

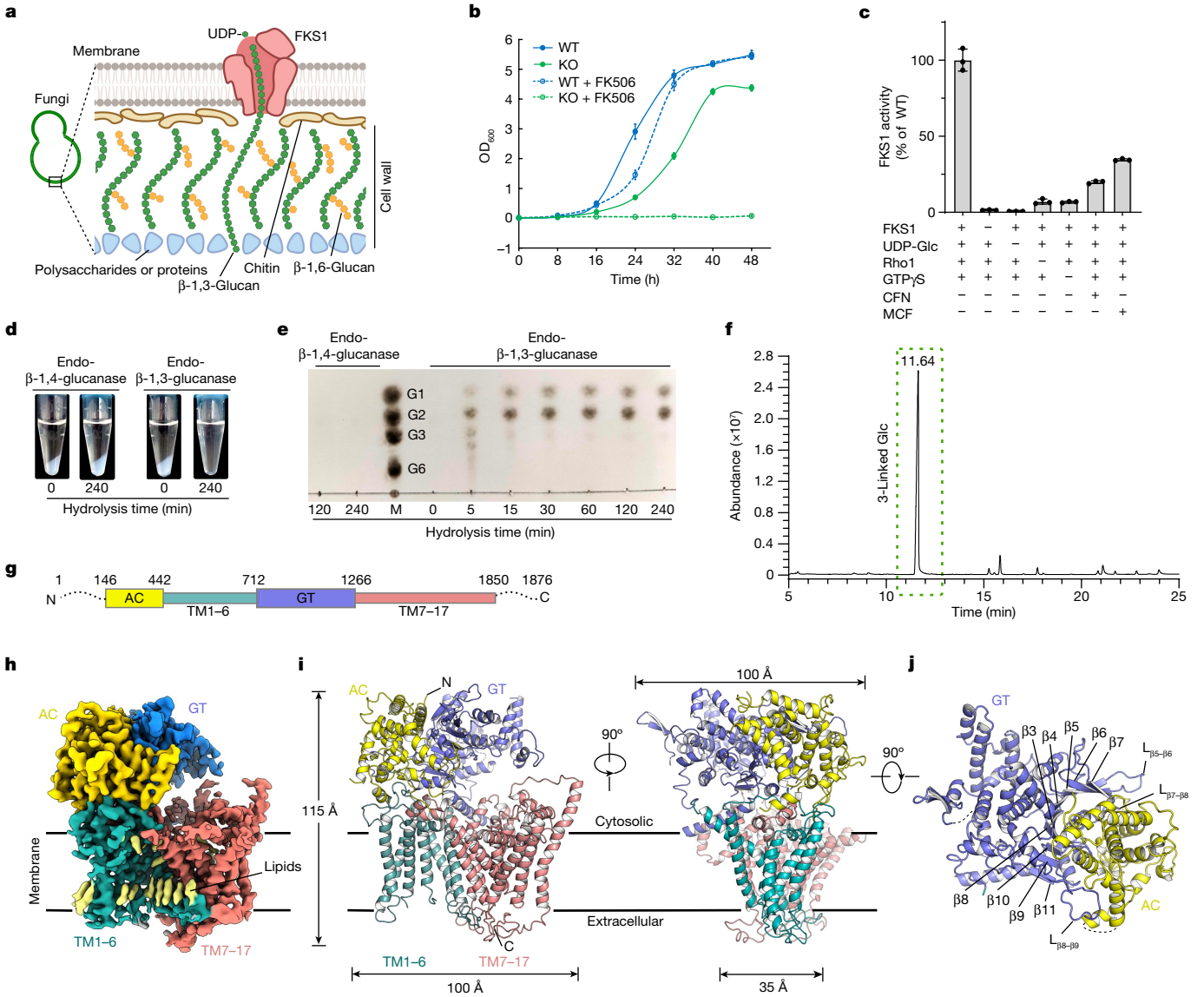

Fig. 1 | Functional and structural characterization of *S. cerevisiae* FKS1. **a**, Model of the fungal cell wall. FKS1 uses UDP-Glc to synthesize β-1,3-glucan. The graphic in panel **a** was created using BioRender (https://biorender.com). **b**, In vivo assay of FKS1 by examining the growth of the WT strain and the *FKS1*-KO (KO) strain with or without the FKS2 inhibitor FK506. Data are mean ± s.e.m.; $n = 3$ independent experiments. **c**, In vitro activity of CHAPS-purified FKS1 with different effectors: UDP-Glc, Rho1, GTPγS and antifungal drugs (caspofungin (CFN) and micafungin (MCF)). Activity was measured by monitoring the UDP generated. Data are mean ± s.e.m.; $n = 3$ independent experiments. **d**,**e**, Enzymatic digestion of the water-insoluble polymer synthesized by GDN-purified FKS1(S643P). Specific endo-1,3-β-glucanase and endo-1,4-β-glucanase were used. These experiments were repeated three times with similar results. A representative image of the polymer digestion (**d**) and hydrolysis samples in **d** withdrawn at indicated times and subject to thin-layer chromatography analysis (**e**) are shown. Glucose (G1), laminaribiose (G2), laminaritriose (G3) and laminarihexaose (G6) were used as the standards (lane M). **f**, Glycosyl linkage (methylation) analysis of the polymer synthesized by GDN-purified FKS1(S643P). A gas chromatogram profile of the partially methylated alditol acetates derived from the synthesized polymers is shown. The dominant peak (outlined by a green dashed box) represents the 1,3-Glc*p* linkage, confirmed by mass spectrometry (Extended Data Fig. 2d). **g**, Schematic of the domain organization of FKS1. **h**, Cryo-EM map of FKS1, viewed parallel to the membrane. The map is segmented into four parts as coloured in **g** with lipid-like densities in light yellow. **i**, Two orthogonal views of the FKS1 structure in cartoon display. Four parts of FKS1 are coloured as in **g**. **j**, Intracellular view of the cytoplasmic region with the TM domain hidden. The central β-sheet of the FKS1 GT domain is composed of β3–β11 as labelled. The dashed lines indicate disordered regions.

growth with the FKS2-specific inhibitor FK506 (refs. [15,24]) (Fig. 1b). By contrast, the *FKS1*-knockout (KO) strain exhibited significantly reduced growth without FK506 and a near total growth inhibition with FK506.

Next, we immunopurified the endogenously expressed *S. cerevisiae* FKS1 in the detergent CHAPS, which is frequently used for the FKS1 activity assay[13,25] (see Methods). Traditionally, FKS activity is measured by a radioactive method on crude membrane or product-entrapped FKS[13,25,26], and here we found that monitoring the UDP generated can make a practical radiolabel-free system for the FKS1 activity assay. FKS1 alone did not exhibit apparent activity. The addition of purified Rho1 in the GTPγS-loaded form dramatically boosted the activity of FKS1 (Fig. 1c), confirming the essential regulatory role of Rho1 on FKS1 (refs. [12,13]). The specific activity of WT FKS1 was determined as approximately 824 nmol min^{-1} mg^{-1}, which is comparable with previous studies[10,25,27]. More importantly, the addition of caspofungin or micafungin, two widely used antifungal drugs that can inhibit β-1,3-glucan synthesis[19], significantly reduced FKS1 activity.

To further confirm the role of FKS1 in β-1,3-glucan synthesis, we analysed the product formed by purified FKS1. For this purpose, we tested WT FKS1 and the variant FKS1(S643P), which is one of the most frequently observed echinocandin-resistant mutations[28]. We hypothesized that the latter variant may alter synthase behaviour. When purified to homogeneity in the detergent GDN (Extended Data Fig. 1a–d and Supplementary Fig. 1), both WT FKS1 and FKS1(S643P) exhibited activity, which can be depleted by immunodepletion (Extended Data Fig. 1h–j). We found that the GDN-purified FKS1 can be activated by caspofungin. Caspofungin can stimulate the activity of FKS1(S643P) (Extended Data Fig. 1h–j). This is further confirmed by scale-up product synthesis in which only FKS1(S643P) with caspofungin produced a significant amount of water-insoluble polymer (Extended Data Fig. 1k). The fact that the enzyme purified in GDN and in CHAPS behaves very differently (Extended Data Fig. 1i versus Fig. 1c) suggests that FKS1 function may be sensitive to membrane environments. The product synthesis by FKS1(S643P) exhibits donor specificity towards the preferred ligand UDP-Glc over UDP-GlcNAc (Extended Data Fig. 1l). Moreover, EDTA can support the catalytic activity of the enzyme and Mg^{2+} significantly inhibited the activity (Extended Data Fig. 1m), consistent with previous studies[25,29,30]. Introduction of a K1261A mutation, an enzyme inactivation mutation discovered from our structural analysis (see the section 'The active site and catalytic mechanism'), to FKS1(S643P) completely inactivated the product synthesis activity of the hyperactive enzyme (Extended Data Fig. 1h–k). The above assays illustrate the specific enzymatic activity of FKS1.

To confirm the formation of the β-1,3-glycosidic linkage, we performed a hydrolysis assay on the synthesized polymer by FKS1(S643P). As a result, endo-1,3-β-glucanase can completely hydrolyse the polymer, whereas endo-1,4-β-glucanase cannot (Fig. 1d and Extended Data Fig. 2a). Thin-layer chromatography analysis showed that the endo-1,3-β-glucanase-catalysed hydrolysate of our synthesized polymer matches the hydrolysate pattern of curdlan (the β-1,3-glucan standard) (Fig. 1e and Extended Data Fig. 2b,c). In addition, methylation glycosyl linkage analysis showed that 1,3-Glc*p* is the dominant linkage in the synthesized polymer (Fig. 1f and Extended Data Fig. 2d). In summary, the above biochemical and chemical studies together firmly establish that FKS1 is a β-1,3-glucan synthase.

Architecture of FKS1

To better understand the mechanism of FKS1, we determined the cryo-EM structure of GDN-purified FKS1 to an overall resolution of 3.4 Å (Fig. 1g,h, Extended Data Table 1 and Extended Data Fig. 3). The density map allowed the de novo building of an atomic model of FKS1 with most residues resolved (Extended Data Fig. 4). To our knowledge, it represents the first structure of the GT48 family membrane-bound GTs.

The overall structure of FKS1 measures approximately 100 Å × 115 Å × 100 Å (Fig. 1i). It contains a transmembrane (TM) domain with 17 TM helices (TM1–17) and a bulky cytoplasmic entity. The TM domain adopts a wedge-like shape, with its narrower end (approximately 35 Å) at the extracellular side. FKS1 has no apparent extracellular structured domains and several elongated loops connect the TM helices. There are several unstructured regions, detailed in the Methods section 'Model building and refinement'.

The cytoplasmic part of FKS1 contains an N-terminal domain and a middle domain, separated by TM1–6 in the primary sequence (Fig. 1g). The middle domain (residues 712–1266) adopts a GT-A fold characteristic of GTs: a continuous central β-sheet of nine strands (β3–β11) surrounded by multiple α-helices[31] (Fig. 1j and Extended Data Fig. 3h). It is therefore named as the GT domain. The N-terminal domain (residues 146–442) contains 14 α-helices (helix 6–7 is not modelled due to lack of densities) (Extended Data Fig. 3i). A search with the Dali server failed to retrieve any structures similar to this domain. Thus, we named it as the accessory (AC) domain. The AC domain interacts extensively with the GT domain, burying a total interface surface area of 2,504 Å^2. Three loops from the GT domain (loop connecting β5 and β6 ($L_{β5–β6}$), $L_{β7–β8}$ and $L_{β8–β9}$) function like plier jaws to clamp the AC domain (Fig. 1j). The highly conserved R319 from the AC domain interacts with N1087 from the GT domain in the domain interface (Extended Data Fig. 3j). The R319A substitution has been previously demonstrated to significantly reduce FKS1 function[24], indicating that the two cytoplasmic domains function together as a compact structural unit.

TM domain of FKS1

Of the total 17 TM helices in FKS1, TM1–8 provide the bulk of the interacting interface with the cytoplasmic entity (Fig. 2a,b and Extended Data Fig. 3i). TM1–4 form a tightly packed helix bundle, contacting TM5–7 on one side (Fig. 2c). TM5–17 are all tilted like open flower petals when viewing from the cytosolic side (Fig. 2a,c). Between the tilted TM5–17 and the GT domain is a large solvent-exposed chamber, which is part of the active site of the enzyme (see below). The TM domain features two membrane-embedded pockets (Fig. 2a). The pocket on the extracellular side is formed because membrane-exposed TM9–10 and TM12 are significantly shorter than typical TM helices. The other pocket on the cytosolic side is formed due to the tilting of TM helices. These two pockets together probably form a path for glucan translocation (see below). Moreover, five long extracellular loops (EL1–5) intertwine to stabilize the close extracellular ends of TM5–17. Two conserved disulfide bonds (C658–C669 on EL1 and C1328–C1345 on EL2) and one potential N-linked glycan on the conserved N1849 are found in these loops (Fig. 2a,b). The tilting of TM5–17 results in large distances between neighbouring helices at the cytosolic end (Fig. 2c). The resulting widespread spaces created are filled in by three lateral helices (LH1–3) parallel to the membrane bilayer: LH1–2 fill the large gap created by two three-helix sheets (TM11, TM12 and TM16; and TM14, TM15 and TM17), whereas LH3 pads the ends of LH1–2.

The resolution of the FKS1 map enabled us to identify multiple orderly bound lipids (Fig. 2a and Extended Data Fig. 4g,h). A phospholipid at the cytosolic membrane leaflet is contacted by TM11, TM15–16 and LH2 (Fig. 2d). Its headgroup is poised to contact the charged residues R1455 (TM11) and R1684 (TM16). Its two lipid alkyl tails pack with surrounding hydrophobic residues: H1654, I1655 and F1658 (TM15); I1680 (TM16); and V1745 and L1746 (LH2). Besides LH1–2, this phospholipid also appears to contribute to the stabilization of the tilted arrangement of the TM helices (Fig. 2a). Other lipid-like densities were modelled as 24 lipid alkyl chains, predominantly located around a core composed of TM5–13 (Fig. 2c). Of these, seven lipids wrap around TM5–6 (Fig. 2c), and 12 form two layers filling in the concave surface created by the tilted TM helices (Fig. 2e). These well-defined lipid molecules are probably part of the integral structure of FKS1.

A 'cellulose-synthase-like fold' in FKS1

Although the architecture of FKS1 is radically different from the membrane-bound GTs with known structures, we noticed that a part of the FKS1 structure (residues 615–1510) resembles the overall topologies of two cellulose synthases of the GT2 family: bacteria BcsA and its plant homologue CesA[32,33] (Fig. 2f–h). Despite their low-sequence identities (less than 10%), FKS1 and BcsA can be superimposed with a root-mean-square-deviation value of 4.3 Å over 308 aligned residues (Extended Data Fig. 5a). A DALI homologous structure search identified two additional structures resembling this topology: hyaluronan synthase (HAS) and dolichylphosphate mannose transferase (PcManGT). Consistently, HAS has been reported with an overall structural similarity to BcsA[34] (Fig. 2i,m); PcManGT has been proposed to contain a minimal cellulose-synthase-like fold with BcsA[35]. These further implicate that these membrane-bound polysaccharide synthases

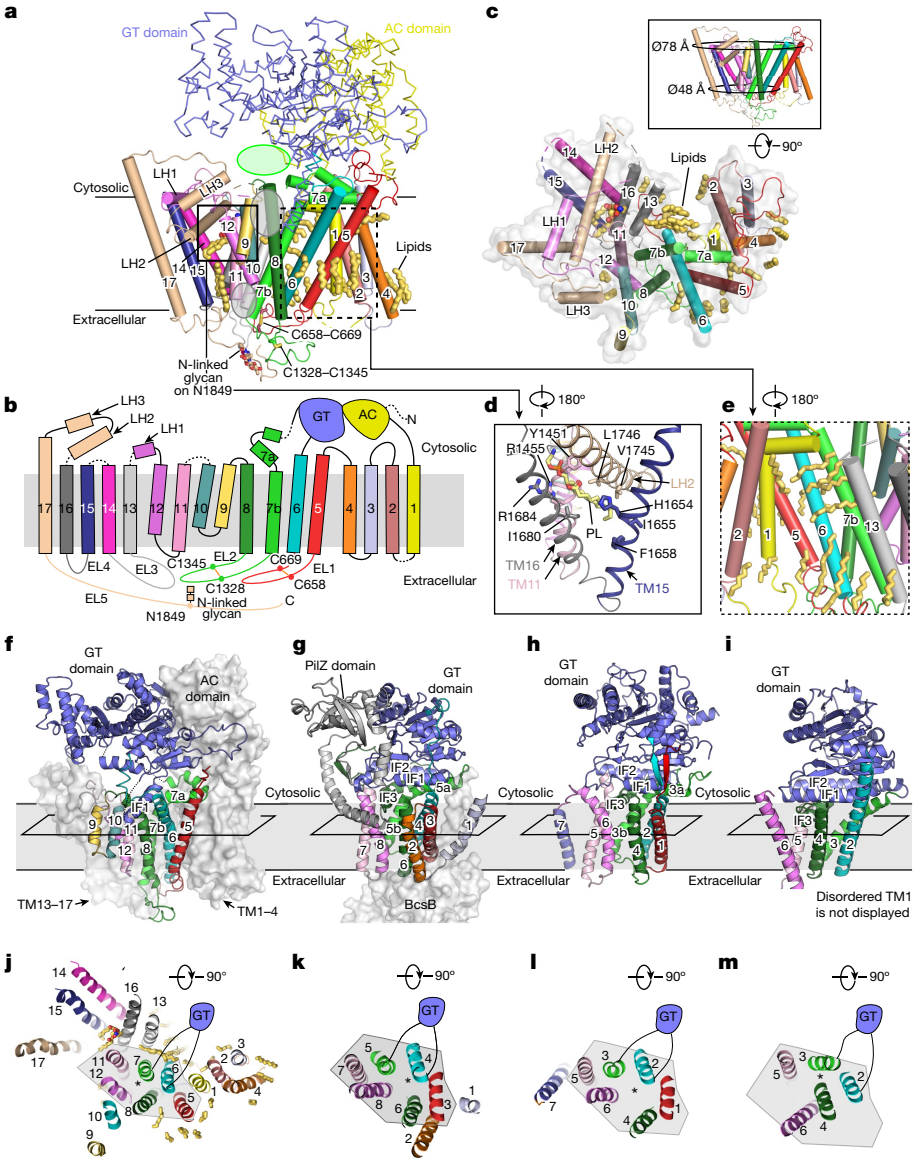

Fig. 2 | The FKS1 TM domain and structural comparison with the cellulose synthases BcsA, CesA and the hyaluronan synthase HAS. a, Front view of FKS1. Seventeen TM helices (denoted by numbers) are in cartoon representation; the cytoplasmic AC and GT domains are in yellow and blue ribbons, respectively. The conserved disulfide bonds at EL1–2 and the N-linked glycan on conserved N1849 of EL5 are labelled. Ordered lipids are in yellow sticks. The three ovals mark the positions of three pockets implicated in catalysis (one green pocket) and glucan translocation (two grey pockets). **b**, Topological diagram of the FKS1 TM domain. The dashed lines depict the flexible elements invisible in the map. **c**, Cytosolic view of the FKS1 TM helices. The inset shows the same view as in **a** with the cytosolic region hidden. The two circles with approximate diameters highlight the tilting of TM5–17, opening towards the cytoplasm. **d**, Residues (shown as sticks) interacting with the internal phospholipid (PL) are outlined by the solid box in **a**. **e**, Back membrane view of the lipid-enriched region outlined by the dashed box in **a**. **f**–**i**, Comparison of the putative shared folds between FKS1 (GT48 family) (**f**) and three membrane-bound synthases of the GT2 family: the bacterial cellulose synthase BcsA (Protein Data Bank (PDB) ID: 4hg6) (**g**), the plant cellulose synthase CesA (PDB ID: 6wlb) (**h**) and the hyaluronan synthase HAS (PDB ID: 7sp7) (**i**). The superimposed structures are shown separately in cartoon representation. Their corresponding elements are in the same colour scheme, whereas elements out of the shared fold are in grey surface or cartoon representation as labelled. In **f**, the dashed lines indicate disordered regions. **j**–**m**, Comparison of the TM arrangements in FKS1 (**j**), BcsA (**k**), CesA (**l**) and HAS (**m**). TM segments in the grey shadow belong to the shared fold. The TM helices are denoted by numbers. The asterisk marks the proposed glucan translocation path in FKS1, BcsA, CesA and HAS.

(FKS1, BcsA, CesA and HAS) may share a core fold, which we refer to as a cellulose-synthase-like fold. This fold shares several features: it is composed of six TM helices, with the GT domain splitting the N-terminal two helices from the C-terminal four helices (Fig. 2j–m); the membrane–cytosol boundary contains several amphipathic interface helices (IFs) (Fig. 2f–i); near this boundary, the TM helix following the GT domain (FKS1 TM7, BcsA TM5, CesA TM3 and HAS TM3) is elongated and has been proposed to line the glucan translocation path[32–34].

Despite the overall resemblance of this modular fold, considerable FKS1-specific features were revealed (Extended Data Fig. 5). The GT domain gains considerate extensions relative to BcsA (Extended Data Fig. 5a,b), and the topologically corresponding TM helices between FKS1 and BcsA vary in orientation and length (Extended Data Fig. 5c). More notable variations are at the membrane–cytoplasm interface. BcsA, CesA and HAS feature three similar amphipathic IFs (IF1–3)[33,34,36] (Fig. 2g–i). In FKS1, the topological counterpart of IF3 becomes TM

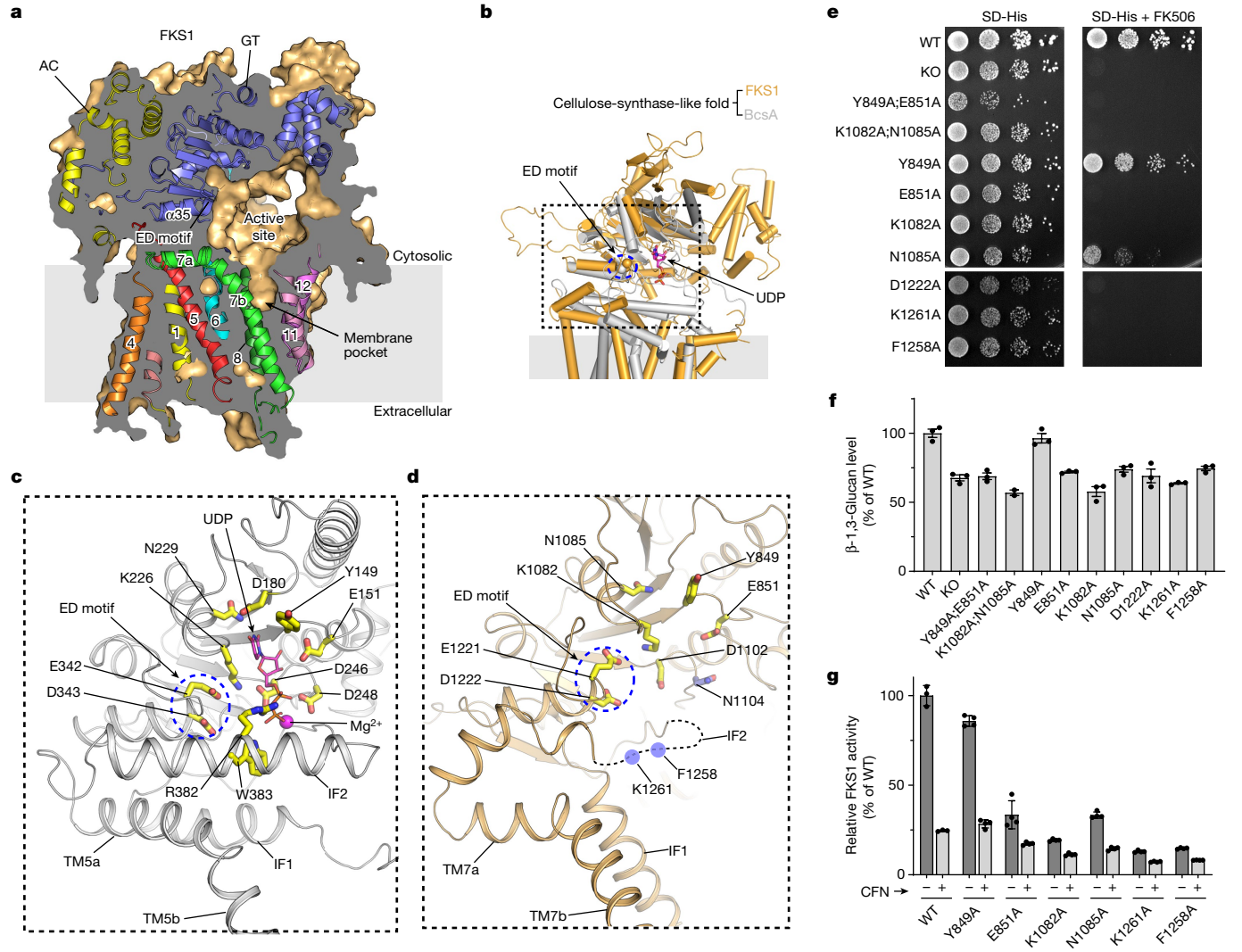

Fig. 3 | The active site of FKS1. a, A cutaway surface representation of FKS1 showing the active site at the membrane–cytoplasm interface. It connects a membrane pocket, which has the potential for glucan translocation. Specific structural elements are shown in cartoon representation, coloured as in Fig. 2a. The TM helices are denoted by numbers. The highly conserved ED motif (E1221 and D1222) located on helix α35 is facing the active site as marked. **b**, Superimposed GT domains of the cellulose-synthase-like folds shared between UDP-bound BcsA (PDB ID: 4P00; in grey with UDP in the magenta stick) and FKS1 (in orange). **c**,**d**, Close-up view of the active sites between BcsA (**c**) and FKS1 (**d**), as marked by the dashed box in **b**. Residues involved in substrate binding or catalysis are indicated as sticks. In **c**, UDP is shown as the magenta stick. In **d**, FKS1 residues conserved with BcsA are highlighted as yellow sticks. **e**, In vivo functional assay of active site mutations in FKS1. The growth of the indicated strains for 72 h was assayed without (left rank) and with (right rank) the FKS2-specific inhibitor FK506. The test was repeated three times with similar results. **f**, Levels of cell wall glucan in strains carrying the indicated FKS1 mutations. **g**, In vitro FKS1 activities of WT and active site mutants purified with CHAPS, with or without the FKS1 inhibitor CFN. Activities were normalized to the amount of protein. For **f**,**g**, data are mean ± s.e.m.; $n = 3$ independent experiments.

helices (TM9–10) instead (Extended Data Fig. 5d,e). Although IF1–2 are preserved in FKS1, they show distinct states. IF1 (that is, helix α33 of the GT domain) of FKS1 rotates almost 90° and is sandwiched between TM6 and TM8 (Extended Data Fig. 5d). IF2 of BcsA corresponds to residues 1247–1266 of FKS1, which are disordered in the map, although predicted as a helix (Extended Data Fig. 5c). This putative FKS1 IF2 lacks the 'QxxRW' motif conserved among BcsA, CesA and HAS[33,34,36] but could still contribute to catalysis, as we discuss later.

The active site and catalytic mechanism

Within the cellulose-synthase-like fold, FKS1 contains a large solvent-exposed chamber at the membrane–cytoplasm interface (Fig. 3a). Alignment of this fold with that of BcsA reveals that the chamber in FKS1 overlaps well with the active site of UDP-bound BcsA, strongly indicating the chamber as the active site of FKS1 (Fig. 3b). A DALI search retrieved homologous structures of the FKS1 GT domain (residues 718–1239): PcManGT, BcsA, GalNAc-T7, TarP, CesA and HAS. We also analysed the AlphaFold model of curdlan synthase because it synthesizes the same polymer as FKS1 and shows high homology (26% identities) with BcsA[37]. Detailed structural comparisons of these targets revealed that the active site of FKS1 overlaps better with membrane-bound enzymes such as BcsA, CesA, curdlan synthase, HAS and PcManGT (Extended Data Fig. 6). Despite the different stereochemistry of their products, the high structural similarity of their active sites indicates similar mechanisms in substrate binding and catalysis of these synthases, consistent with previous studies of BcsA, CesA and HAS[33,34,36]. On the basis of these insights, we overlaid the structures of FKS1 and BcsA to reveal the shared key functionally important residues in their active sites (Fig. 3c,d). For example, two pairs of residues (Y849 and

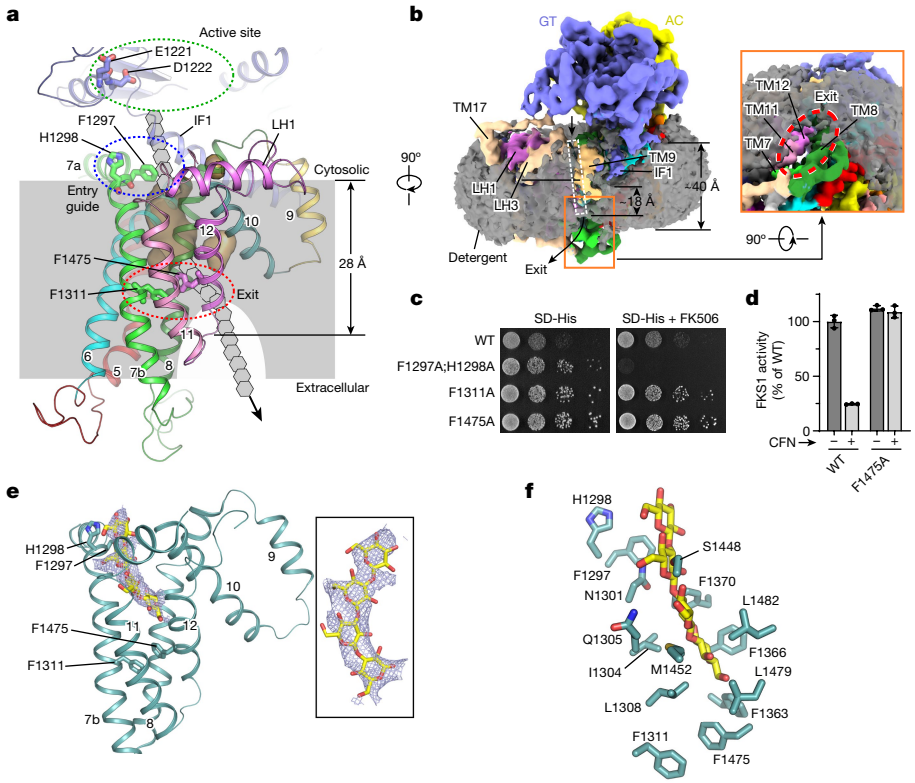

Fig. 4 | Putative glucan translocation path. a, Putative glucan translocation path through two membrane pockets as illustrated by the hexagon array. The first pocket (in the internal shaded surface view), lined by TM5–12, is located under the active site (green dashed oval). Conserved residues implicated in guiding the entrance (H1298 and F1297) and sealing the exit (F1311 and F1475) are labelled. At the extracellular side, a second pocket is formed because membrane-exposed TM9–10 and TM12 are too short (less than 28 Å) to span the whole membrane. **b**, Unsharpened EM density map shows the detergent depression close to the glucan translocation path. This path is marked by the white dashed box, with the arrows indicating the putative entrance and exit. The detergent density is in grey. The estimated membrane thickness is labelled. The inset shows the extracellular view of the region boxed with the orange line. **c**, In vivo functional assay of FKS1 with selected mutations around the glucan translocation path. The growth of the indicated strains for 48 h were assayed without (left) and with (right) the FKS2-specific inhibitor FK506. **d**, In vitro FKS1 activities of the WT and the F1475A mutant purified with CHAPS, with or without the FKS1 inhibitor CFN. Activities were normalized to the amount of protein. Data are mean ± s.e.m.; $n = 3$ independent experiments. **e**, Structure of FKS1(S643P) shows an elongated density (blue mesh) in the first membrane pocket (as shown in **a**) for product translocation. This structure was determined in the presence of UDP-Glc to synthesize product, which was boosted by CFN. The TM helices are denoted by numbers. The inset shows the zoomed-in view of a modelled glucan chain of 4-glucose (yellow stick) superimposed with its corresponding density (blue mesh). **f**, Potential residues involved in glucan interaction.

E851, and K1082 and N1085 in FKS1; Y149 and E151, and K226 and N229 in BcsA) and the 'ED motif' (E1221 and D1222 in FKS1; and E342 and D343 in BcsA) in the two enzymes can be aligned well. These residues in BcsA are known for donor binding (Y149 and E151, and K226 and N229 in BcsA) and for positioning the general catalytic base aspartate (ED motif)[36].

Next, we validated the functional roles of these residues using three different assays. First, we introduced their mutations into the *FKS1* chromosomal locus and assayed the growth phenotype of each mutant strain in the presence of FK506 (Fig. 3e). The double mutations of Y849A;E851A and K1082A;N1085A and the single mutations of E851A, K1082A and D1222A all prevented strain growth to the extent of the *FKS1*-KO strain (Fig. 3e). The N1085A mutation slowed growth and the Y849A mutation did not have an obvious effect on growth. Second, we measured the levels of cell wall glucan in these strains when growing without FK506. We found that all mutations, including the *FKS1*-KO strain but except for the Y849A substitution, decreased the overall levels of glucan compared with the WT strain (Fig. 3f), matching well with their growth phenotypes (Fig. 3e). Last, we purified every single FKS1 mutant (except for FKS1(D1222A)) and compared their catalytic activity in vitro (Fig. 3g and Extended Data Fig. 1g). Consistent with the cell-based phenotypes described above, the E851A, K1082A and N1085A mutations significantly reduced the enzyme activity, whereas the Y849A mutation only mildly affected the activity. Together, the above in vivo and in vitro analyses firmly establish the location of the FKS1 active site as well as its key composing residues.

Further structural analysis allowed us to identify additional residues critical for FKS1 catalysis. R382 and W383 in the 'QxxRW' motif in IF2 of BcsA is known to be important for substrate binding and catalysis[36]. Although this motif is missing in FKS1, K1261 and F1258 are located at the corresponding positions in FKS1, as R382 and W383 do in BcsA (Fig. 3c,d and Extended Data Fig. 5e). In multiple membrane-bound synthases containing the cellulose-synthase-like fold (BcsA, CesA and HAS), the positively charged residue corresponding to BcsA R382 is involved in donor binding, whereas the aromatic residue corresponding to BcsA W383 functions to stabilize the acceptor[33,34,36] (Extended Data Fig. 6). Indeed, both F1258 and K1261 are essential for FKS1 function, as demonstrated by the in vivo and in vitro analyses of their single alanine mutations (Fig. 3e–g). The above analyses further suggest that the core catalytic mechanisms between FKS1 and BcsA are conserved.

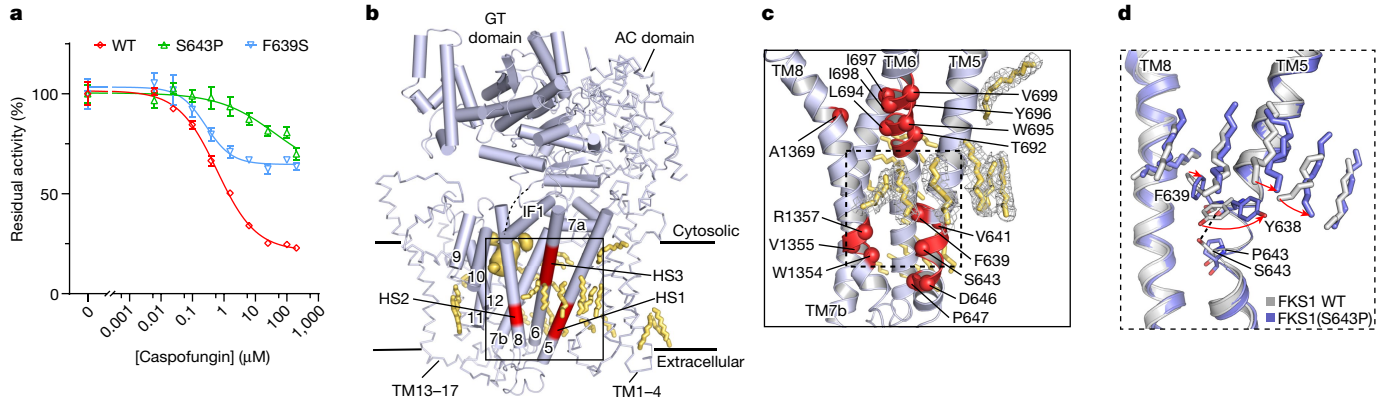

Fig. 5 | Structural interpretation of echinocandin-resistant or ibrexafungerp-resistant mutations. a, CFN inhibition profiles of FKS1 variants purified with CHAPS, including WT FKS1 and two most frequently observed echinocandin-resistant mutations: F639S and S643P. The percentage of residual activity is shown. Data are mean ± s.e.m.; $n = 3$ independent experiments. **b**, Three hotspot regions (red; denoted as HS1–3) with echinocandin-resistant mutations are mapped onto the FKS1 structure. The hotspot regions are localized on a cluster of three neighbouring TM helices: TM5, TM8 and TM6, respectively. The conserved cellulose-synthase-like fold within FKS1 is highlighted in cartoon representation, whereas the remaining part is in ribbon representation. This conserved fold is surrounded by ordered lipids shown as yellow sticks. The dashed line indicates disordered region. **c**, Close-up view of the echinocandin-resistant mutations as outlined in **b**. An ibrexafungerp-resistant mutation site (A1369) outside these hotspot regions is also shown. The Cα atoms of the mutations are denoted as red spheres. The hotspot regions are enriched with ordered lipids, with selected lipid densities shown in a grey mesh. **d**, Conformational changes and lipid arrangements (indicated by red arrows) around the HS1 region due to the introduction of FKS1(S643P), the drug-resistant mutation. This is illustrated by the overlay of the FKS1 structure (grey) and the FKS1(S643P) structure (blue). The black dashed line indicates a potential polar interaction.

The putative glucan translocation path

FKS1 and BcsA are both processive polysaccharide synthases and their polymerized product, glucans, need to be translocated across membranes[1,38]. In accordance with this, right below the active site, FKS1 has a pocket formed within the membrane (Fig. 3a). It is lined by TM5–8, TM11–12 and IF1 (Fig. 4a). TM5–8 and TM11–12 of FKS1 are part of the cellulose-synthase-like fold core and they correspond to TM3–8 forming the cellulose translocation path in BcsA[36] (Fig. 2j,k). At the extracellular side opposite to this pocket, there exists another solvent exposed pocket with much lower detergent density that is directly visible from the EM map (Fig. 4b). The second pocket is formed because the membrane-exposed TM9–10 and TM12 are short. The two juxtaposed hydrophilic pockets with the membrane plane lead to notable membrane thinning (Fig. 4a,b), which could greatly reduce the energy barrier for glucan translocation across the membranes, as has been proposed for several membrane translocases[39]. Indeed, mutations of residues along this path in FKS1 altered FKS1 function (Fig. 4c,d). For example, two conserved residues (F1297 and H1298) are located between the active site and the cytosolic entrance. Their alanine substitutions impaired FKS1 function, suggesting that they may be involved in glucan guiding. By contrast, when substituting two conserved bulky aromatic residues sealing the extracellular exit (F1311 and F1475) with alanine, the mutant strains grew faster than the WT strain. We were able to purify FKS1(F1475A) and it exhibited increased in vitro catalytic activity and reduced sensitivity to the FKS1 inhibitor caspofungin (Fig. 4d), implying the enlargement of F1475A in the glucan exit.

We next determined the structure of the GDN-purified hyperactive mutant FKS1(S643P) when incubated with UDP-Glc and caspofungin, to the resolution of 3.5 Å (Extended Data Fig. 7), hoping to capture the substrate-bound or product-bound state of the enzyme. Although the structure of FKS1(S643P) shows no large conformational differences from that of WT FKS1 (root-mean-square deviation of approximately 0.7 Å), we noticed an elongated density along the proposed product translocation channel in it, presumably corresponding to a bound product (Fig. 4e). We modelled a glucan chain of 4-glucose into this density (Fig. 4e, inset). A series of hydrophilic and hydrophobic residues from FKS1 are lined along the modelled glucan chain for favourable enzyme–product interactions (Fig. 4f). The translocation channel remains closed at the extracellular side, suggesting the existence of a regulated channel opening mechanism, as has been recently proposed for HAS[34].

Implications for echinocandin resistance

We first evaluated our *S. cerevisiae*-based assay system for the analysis of echinocandin resistance. We selected two most frequently observed mutations in drug-resistant *C. albicans* (*Ca*FKS1 F641S and S645P)[28] and introduced them into the corresponding sites of *S. cerevisiae* FKS1 (*Sc*FKS1 F639S and S643P). Both mutant strains exhibited highly elevated resistance to caspofungin (Extended Data Fig. 8a). We further purified these two mutated *Sc*FKS1 in CHAPS and evaluated their inhibition by caspofungin (Fig. 5a). The WT *Sc*FKS1 as control exhibited a typical inhibitory profile, with the IC_{50} determined as 0.55 μM, which is comparable with that determined previously with different methods[23,25]. By contrast, both *Sc*FKS1(F639S) and *Sc*FKS1(S643P) are insensitive to inhibition by caspofungin.

Next, we investigated the possible mechanistic basis of echinocandin-resistance using the FKS1 structure. According to their locations, echinocandin-resistant mutations were categorized into three conserved regions, encompassing residues 639–647 in TM5 (hotspot 1), 1354–1357 in TM8 (hotspot 2) and 690–700 in TM6 (hotspot 3) (residues are numbered as in *Sc*FKS1)[20,22,40] (Supplementary Fig. 2). Although separated in the primary sequence, three mutation hotspots are spatially close to each other (Fig. 5b,c). In *C. glabrata* isolates resistant to ibrexafungerp, new mutation sites outside FKS2 hotspots 1 and 2 were reported (for example, *Cg*FKS2 W715L and A1390D)[41]; these mutation sites correspond to W695 in hotspot 3 of *Sc*FKS1 and A1369 on TM8 adjacent to hotspot 3, respectively (Fig. 5c). This analysis suggests overlapping FKS-binding sites between echinocandin and ibrexafungerp[41]. These drug-resistant hotspot regions appear to be closely related to the membrane environment.

All echinocandin-resistant mutations of FKS1 are mapped near the convex hydrophobic surface formed by TM5–6 and TM8 and are specifically surrounded by several ordered lipid molecules (Figs. 2c and 5c). F639 and S643 of the hotspot 1 region are involved in lipid binding; the side chain of F639 directly interacts with three lipid molecules and the S643 side chain appears to fix the main chain of the lipid-interacting residue Y638 (Fig. 5d). Furthermore, we analysed the structure of FKS1(S643P) (Extended Data Fig. 7), focusing on alterations of lipid binding induced by the mutation (Fig. 5d). Several hotspot 1 residues near the enriched lipids show altered conformation; Y638 has its side chain rotated approximately 90°, with the F639 side chain rotating in the same direction. Remarkably, these changes lead to shifts of nearby bound lipids, suggesting that an altered lipid environment resulted from the S643P mutation.

On the basis of our results, we propose two possible drug-resistant mechanisms for FKS1. First, as the echinocandin-type drugs are lipopeptides with differently configured lipid tails[19] (Extended Data Fig. 8b,c), the clustering pattern of the echinocandin-resistant mutations suggests a possible binding site for these drugs, and the bindings may involve their lipid tails (Fig. 5b,c). The drug resistance may hence be attributed to alterations of the drug-binding site that resulted from the mutations. Second, considering the enriched ordered lipids near drug-resistant hotspot regions and the lipid movements revealed from the structure of FKS1(S643P) (Fig. 5c,d), it is conceivable that the drug-resistant mutations could alter the response of FKS1 to membrane changes caused by echinocandin. Such a mechanism has been proposed for the antibiotics daptomycin and polymyxins, which are also lipopeptide drugs and membrane-acting[42,43]. Consistently, it has been reported that specific membrane microdomains are associated with the synthesis of β-1,3-glucan[44,45]. In addition, changes in the lipid microenvironment have been demonstrated to correlate with the action of echinocandin on FKS[46,47].

Conclusions

Our work reveals the molecular architecture of the fungal glucan synthase FKS1. The structures of FKS1, together with extensive functional characterizations, advance our mechanistic understanding of fungal cell wall β-1,3-glucan synthesis. Structure-based analysis of echinocandin-resistant mutations and the structure of the S643P mutant suggest a plausible drug-resistant mechanism of the FKS1 mutations. These insights may also be shared by various fungal pathogens as their FKS orthologues are highly conserved (Extended Data Fig. 9 and Supplementary Fig. 2). The FKS1 structures and the catalytic mechanism elucidated in this work may serve as a framework for future studies of this important antifungal drug target, as well as for screening and the development of new antifungal agents.

Online content

Any methods, additional references, Nature Portfolio reporting summaries, source data, extended data, supplementary information, acknowledgements, peer review information; details of author contributions and competing interests; and statements of data and code availability are available at https://doi.org/10.1038/s41586-023-05856-5.

1. Wagener, J., Striegler, K. & Wagener, N. α- and β-1,3-Glucan synthesis and remodeling. *Curr. Top. Microbiol. Immunol.* **425**, 53–82 (2020).
2. Gow, N. A. R., Latge, J. P. & Munro, C. A. The fungal cell wall: structure, biosynthesis, and function. *Microbiol. Spect.* https://doi.org/10.1128/microbiolspec.FUNK-0035-2016 (2017).
3. Perfect, J. R. The antifungal pipeline: a reality check. *Nat. Rev. Drug Discov.* **16**, 603–616 (2017).
4. Hoenigl, M. et al. The antifungal pipeline: fosmanogepix, ibrexafungerp, olorofim, opelconazole, and rezafungin. *Drugs* **81**, 1703–1729 (2021).
5. Brown, G. D. et al. Hidden killers: human fungal infections. *Sci. Transl. Med.* **4**, 165rv113 (2012).
6. Hoenigl, M. Invasive fungal disease complicating COVID-19: when it rains it pours. *Clin. Infect. Dis.* **73**, e1645–e1648 (2021).
7. Perlin, D. S., Rautemaa-Richardson, R. & Alastruey-Izquierdo, A. The global problem of antifungal resistance: prevalence, mechanisms, and management. *Lancet Infect. Dis.* **17**, e383–e392 (2017).
8. Fisher, M. C., Hawkins, N. J., Sanglard, D. & Gurr, S. J. Worldwide emergence of resistance to antifungal drugs challenges human health and food security. *Science* **360**, 739–742 (2018).
9. Perlin, D. S. Cell wall-modifying antifungal drugs. *Curr. Top. Microbiol. Immunol.* **425**, 255–275 (2020).
10. Inoue, S. B. et al. Characterization and gene cloning of 1,3-β-D-glucan synthase from *Saccharomyces cerevisiae*. *Eur. J. Biochem.* **231**, 845–854 (1995).
11. Douglas, C. M. et al. The *Saccharomyces cerevisiae* FKS1 (ETG1) gene encodes an integral membrane protein which is a subunit of 1,3-β-D-glucan synthase. *Proc. Natl Acad. Sci. USA* **91**, 12907–12911 (1994).
12. Qadota, H. et al. Identification of yeast Rho1p GTPase as a regulatory subunit of 1,3-β-glucan synthase. *Science* **272**, 279–281 (1996).
13. Mazur, P. & Baginsky, W. In vitro activity of 1,3-β-D-glucan synthase requires the GTP-binding protein Rho1. *J. Biol. Chem.* **271**, 14604–14609 (1996).
14. Katiyar, S. K. et al. Fks1 and Fks2 are functionally redundant but differentially regulated in *Candida glabrata*: implications for echinocandin resistance. *Antimicrob. Agents Chemother.* **56**, 6304–6309 (2012).
15. Mazur, P. et al. Differential expression and function of two homologous subunits of yeast 1,3-β-D-glucan synthase. *Mol. Cell. Biol.* **15**, 5671–5681 (1995).
16. Thompson, J. R. et al. A glucan synthase FKS1 homolog in *Cryptococcus neoformans* is single copy and encodes an essential function. *J. Bacteriol.* **181**, 444–453 (1999).
17. Douglas, C. M. et al. Identification of the FKS1 gene of *Candida albicans* as the essential target of 1,3-β-D-glucan synthase inhibitors. *Antimicrob. Agents Chemother.* **41**, 2471–2479 (1997).
18. Dichtl, K. et al. *Aspergillus fumigatus* devoid of cell wall β-1,3-glucan is viable, massively sheds galactomannan and is killed by septum formation inhibitors. *Mol. Microbiol.* **95**, 458–471 (2015).
19. Chen, S. C., Slavin, M. A. & Sorrell, T. C. Echinocandin antifungal drugs in fungal infections: a comparison. *Drugs* **71**, 11–41 (2011).
20. Perlin, D. S. Mechanisms of echinocandin antifungal drug resistance. *Ann. N.Y. Acad. Sci.* **1354**, 1–11 (2015).
21. Alexander, B. D. et al. Increasing echinocandin resistance in *Candida glabrata*: clinical failure correlates with presence of FKS mutations and elevated minimum inhibitory concentrations. *Clin. Infect. Dis.* **56**, 1724–1732 (2013).
22. Johnson, M. E., Katiyar, S. K. & Edlind, T. D. New Fks hot spot for acquired echinocandin resistance in *Saccharomyces cerevisiae* and its contribution to intrinsic resistance of *Scedosporium* species. *Antimicrob. Agents Chemother.* **55**, 3774–3781 (2011).
23. Park, S. et al. Specific substitutions in the echinocandin target Fks1p account for reduced susceptibility of rare laboratory and clinical *Candida* sp. isolates. *Antimicrob. Agents Chemother.* **49**, 3264–3273 (2005).
24. Johnson, M. E. & Edlind, T. D. Topological and mutational analysis of *Saccharomyces cerevisiae* Fks1. *Eukaryot. Cell* **11**, 952–960 (2012).
25. Chhetri, A. et al. Length specificity and polymerization mechanism of (1,3)-β-D-glucan synthase in fungal cell wall biosynthesis. *Biochemistry* **59**, 682–693 (2020).
26. Suwunnakorn, S., Wakabayashi, H., Kordalewska, M., Perlin, D. S. & Rustchenko, E. FKS2 and FKS3 genes of opportunistic human pathogen *Candida albicans* influence echinocandin susceptibility. *Antimicrob. Agents Chemother.* **62**, e02299-17 (2018).
27. Beauvais, A. et al. Glucan synthase complex of *Aspergillus fumigatus*. *J. Bacteriol.* **183**, 2273–2279 (2001).
28. Perlin, D. S. Echinocandin resistance, susceptibility testing and prophylaxis: implications for patient management. *Drugs* **74**, 1573–1585 (2014).
29. Mullins, J. T. Regulatory mechanisms of β-glucan synthases in bacteria, fungi, and plants. *Physiol. Plant.* **78**, 309–314 (1990).
30. Frost, D. J., Brandt, K., Capobianco, J. & Goldman, R. Characterization of (1,3)-β-glucan synthase in *Candida albicans*: microsomal assay from the yeast or mycelial morphological forms and a permeabilized whole-cell assay. *Microbiology* **140**, 2239–2246 (1994).
31. Lairson, L. L., Henrissat, B., Davies, G. J. & Withers, S. G. Glycosyltransferases: structures, functions, and mechanisms. *Annu. Rev. Biochem.* **77**, 521–555 (2008).
32. Morgan, J. L., McNamara, J. T. & Zimmer, J. Mechanism of activation of bacterial cellulose synthase by cyclic di-GMP. *Nat. Struct. Mol. Biol.* **21**, 489–496 (2014).
33. Purushotham, P., Ho, R. & Zimmer, J. Architecture of a catalytically active homotrimeric plant cellulose synthase complex. *Science* **369**, 1089–1094 (2020).
34. Maloney, F. P. et al. Structure, substrate recognition and initiation of hyaluronan synthase. *Nature* **604**, 195–201 (2022).
35. Gandini, R. et al. A transmembrane crenarchaeal mannosyltransferase is involved in N-glycan biosynthesis and displays an unexpected minimal cellulose-synthase-like fold. *J. Mol. Biol.* **432**, 4658–4672 (2020).
36. Morgan, J. L., Strumillo, J. & Zimmer, J. Crystallographic snapshot of cellulose synthesis and membrane translocation. *Nature* **493**, 181–186 (2013).
37. Stasinopoulos, S. J., Fisher, P. R., Stone, B. A. & Stanisich, V. A. Detection of two loci involved in (1→3)-β-glucan (curdlan) biosynthesis by *Agrobacterium* sp. ATCC31749, and comparative sequence analysis of the putative curdlan synthase gene. *Glycobiology* **9**, 31–41 (1999).
38. Bi, Y., Hubbard, C., Purushotham, P. & Zimmer, J. Insights into the structure and function of membrane-integrated processive glycosyltransferases. *Curr. Opin. Struct. Biol.* **34**, 78–86 (2015).
39. Wu, X. D. & Rapoport, T. A. Translocation of proteins through a distorted lipid bilayer. *Trends Cell Biol.* **31**, 473–484 (2021).
40. Carolus, H. et al. Genome-wide analysis of experimentally evolved *Candida auris* reveals multiple novel mechanisms of multidrug resistance. *mBio* **12**, e03333-20 (2021).

41. Jimenez-Ortigosa, C., Perez, W. B., Angulo, D., Borroto-Esoda, K. & Perlin, D. S. De novo acquisition of resistance to SCY-078 in *Candida glabrata* involves FKS mutations that both overlap and are distinct from those conferring echinocandin resistance. *Antimicrob. Agents Chemother.* **61**, e00833-17 (2017).
42. Muller, A. et al. Daptomycin inhibits cell envelope synthesis by interfering with fluid membrane microdomains. *Proc. Natl Acad. Sci. USA* **113**, E7077–E7086 (2016).
43. Lewis, K. The science of antibiotic discovery. *Cell* **181**, 29–45 (2020).
44. Bessueille, L. et al. Plasma membrane microdomains from hybrid aspen cells are involved in cell wall polysaccharide biosynthesis. *Biochem. J.* **420**, 93–103 (2009).
45. Briolay, A. et al. Cell wall polysaccharide synthases are located in detergent-resistant membrane microdomains in oomycetes. *Appl. Environ. Microbiol.* **75**, 1938–1949 (2009).
46. Healey, K. R., Katiyar, S. K., Raj, S. & Edlind, T. D. CRS-MIS in *Candida glabrata*: sphingolipids modulate echinocandin–Fks interaction. *Mol. Microbiol.* **86**, 303–313 (2012).
47. Satish, S. et al. Stress-induced changes in the lipid microenvironment of β-(1,3)-D-glucan synthase cause clinically important echinocandin resistance in *Aspergillus fumigatus*. *mBio* **10**, e00779-19 (2019).

Methods

Expression and purification of FKS1

A 3× Flag tag was engineered to the C terminus of chromosomal FKS1 on *S. cerevisiae* strain BY4742, using a PCR-based tagging method[48]. A yeast strain with the FKS1(S643P) chromosomal mutation was generated using the homologous recombination method[49]. For cryo-EM analysis and product synthesis, FKS1 and the FKS1(S643P) mutant were purified with detergent GDN as described below. The strains were cultured in YPD medium at 30 °C for 20 h. Cells were collected by centrifugation and lysed by French Press in lysis buffer containing 50 mM Tris-HCl pH 7.4, 150 mM NaCl and 2 mM $MgCl_2$ supplemented with 1 mM phenylmethane sulphonylfluoride (PMSF). The lysate was centrifuged at 15,000*g* for 30 min. The supernatant was subject to ultracentrifugation at 100,000*g* for 1 h. The collected membrane pellet was solubilized in buffer 50 mM Tris-HCl pH 7.4, 500 mM NaCl, 2 mM $MgCl_2$, 10% (v/v) glycerol, 1.5% (w/v) *n*-dodecyl-β-D-maltopyranoside (DDM; Anatrace), 0.15% cholesteryl hemisuccinate Tris salt (CHS; Anatrace) and protease inhibitor (cOmplete protease inhibitor cocktail; Roche) by gentle agitation for 2 h. Supernatant was collected by centrifugation at 15,000*g* for 0.5 h and was applied to Anti-Flag M2 affinity gel (Sigma). The gel was then washed with washing buffer containing 50 mM Tris-HCl pH 7.4, 150 mM NaCl, 2 mM $MgCl_2$ and 0.04% GDN (Anatrace). The target proteins were eluted with washing buffer supplemented with 150 μg ml^{-1} 3× Flag peptide. The eluate was concentrated and further purified using size-exclusion chromatography (Superose 6 10/300 GL column, GE Healthcare) with buffer containing 50 mM Tris-HCl pH 7.4, 150 mM NaCl, 2 mM $MgCl_2$ and 0.04% GDN (Anatrace). The central fractions of monodisperse peak were collected and concentrated for cryo-EM grid preparation and product synthesis.

Expression and purification of Rho1

The vector construction of N-terminal 6× His-SUMO-tagged *S. cerevisiae* Rho1 was transformed into *Escherichia coli* BL21(DE3). The strains were cultured in LB medium supplemented with 100 μg ml^{-1} ampicillin at 37 °C till OD_{600} reached approximately 0.6. Protein expression was induced with 0.5 mM isopropyl-β-D-1-thiogalactopyranoside at 18 °C for 20 h. The collected bacteria were resuspended and lysed by French Press in buffer A containing 50 mM Tris-HCl pH 7.4, 300 mM NaCl and 2 mM $MgCl_2$. After centrifugation, the protein was purified from the supernatant using nickel–nitrilotriacetic acid (Ni–NTA) affinity chromatography. When dialysing into buffer A, 6× His-tagged protease Ulp1 at a 1:200 Ulp1:Rho1 (w/w) ratio was added to remove the 6× His-SUMO tag. The cleaved 6× His-SUMO tag and the protease were removed by another run of Ni–NTA affinity chromatography, and the flow-through was collected, concentrated and subjected to a gel-filtration chromatography (Superdex 200, GE Healthcare) in buffer containing 50 mM Tris-HCl pH 7.4, 150 mM NaCl and 2 mM $MgCl_2$. The central fractions of the monodisperse peak at 15.6 ml were collected and concentrated to 10 mg ml^{-1}.

Cryo-EM data acquisition

For single-particle cryo-EM analysis, a 3 μl aliquot of the purified FKS1 at a concentration of 5 mg ml^{-1} was applied to glow-discharged Quantifoil carbon grids (R1.2/1.3 Au, 300 mesh). The grids were blotted for 4 s at 100% humidity and flash frozen in liquid ethane using FEI Vitrobot IV. For the UDP-Glc-incubated FKS1(S643P) sample, FKS1(S643P) purified in GDN (7 mg ml^{-1}) was mixed with UDP-Glc (0.5 mM), supplemented with 0.7 mg ml^{-1} Rho1, 10 μM GTPγS, 200 μM caspofungin, 0.1% CHAPS and 0.02% CHS. The mixture was incubated at 16 °C for 2 h before freezing the cryo-EM grids. Cryo-EM data were collected on a FEI Titan Krios electron microscopy operated at 300 kV equipped with a Gatan K3 Summit camera positioned after a GIF quantum energy filter. Automated data acquisition was performed with SerialEM or FEI EPU. Micrographs were recorded under super-resolution counting mode at a nominal magnification of ×130,000, in a physical pixel size of 0.92 Å per pixel. Defocus values ranged from −1.2 μm to −3 μm. A total exposure of 1.3 s was dose-fractionated into 32 frames, resulting in a total accumulated dose of 50 e^- per $Å^2$.

Image processing and 3D reconstruction

The dose-fractionated movies recorded were first aligned and dose-weighted with MotionCor2 (ref. [50]). CTFFIND4 was then used to determine the contrast transfer function parameters for individual micrographs[51]. Low-quality micrographs revealed by manual inspection were excluded from further analysis. Subsequent image-processing steps were performed using RELION-3 (ref. [52]).

For the FKS1 dataset, a set of 2,000 particles were manually selected to generate 2D class templates for reference-based automatic particle picking. The automatic picking yielded in 2,321,905 particles from 11,606 micrographs. Two rounds of reference-free 2D classification were performed to remove particles with poor quality, resulting in a cleaned set of 1,335,014 particles. An ab initio map was generated with RELION and was used as the initial reference model for further 3D classification. After three rounds of 3D classification, a 3D class with high-resolution features (267,574 particles) was selected. Subsequent particle polishing, 3D refinement and post-processing generated a map with an overall resolution of 3.4 Å.

For the FKS1(S643P) dataset, a set of approximately 2,000 particles were manually selected to generate 2D class templates for reference-based automatic particle picking. The automatic picking yielded in 2,222,315 particles from 9,623 micrographs. Two rounds of reference-free 2D classification were performed to remove particles with poor quality, resulting in a cleaned set of 1,620,308 particles. The FKS1 model was used as the initial reference model for further 3D classification. A 3D class with high-resolution features (690,251 particles) was selected. Subsequent particle polishing, 3D refinement and post-processing generated a map with an overall resolution of 3.6 Å. This reconstruction revealed fragment density within the product translocation channel, indicating a mixed state with or without bound product. Therefore, we performed an additional round of focused 3D classification without particle realignment, using a focused mask around TM7–12 and the active site that surround the translocation channel. A 3D class with highest resolution features (176,682 particles) was selected. The selected particles were re-extracted for 3D refinement with full mask and subsequent post-processing. This generated a map with an overall resolution of 3.5 Å, which was used to build the FKS1(S643P) model.

The overall resolutions were estimated based on the gold-standard Fourier shell correlation 0.143 criterion[53]. Local resolution distribution was estimated using ResMap[54].

Model building and refinement

A rough initial model of FKS1 was generated de novo using the map_to_model module in PHENIX[55]. It was further improved by manual adjustments and rebuilding using Coot[56], which was facilitated by the good densities around the TM helices and bulky densities around residues such as Trp, Tyr, Phe and Arg. The refinement of the FKS1 model against the cryo-EM map in real space was carried out in PHENIX with secondary structure and geometry restraints[55]. In the final FKS1 model, there are several unstructured regions, including N-terminal 145 residues, C-terminal 16 residues, six flexible segments of cytoplasmic domain (residues 244–278, 475–487, 798–805, 897–931, 1159–1167 and 1247–1266) and four loop segments to connect TM helices (residues 1419–1435, 1516–1554, 1627–1637 and 1698–1723). The model of FKS1(S643P) was built based on the model of FKS1. MOLPROBITY was used to assess the final model[57]. The Fourier shell correlation between the model and the map was calculated by PHENIX.mtriage[58]. The homologous structure search was performed using the DALI server[59]. For structural comparison with FKS1, the AlphaFold-modelled structure of curdlan

synthase was used[60,61]. The illustrated figures were prepared using PyMOL (Schrödinger, LLC), Chimera and ChimeraX[62,63]. Statistics of the 3D reconstructions and model refinements are shown in Extended Data Table 1.

Spot growth assay

Yeast strains with FKS1 chromosomal mutations and the *FKS1*-KO strain were generated using the homologous recombination method[49]. The mutants were selected on SD-His (Yeast Synthetic Drop-out Medium without Histidine, cat no. S0020, Solarbio) and were confirmed by genomic PCR and DNA sequencing. For the analysis of growth phenotype, the spot growth assay of mutated strains was adapted from a previously described method[24]. The strains were cultured in YPD media at 30 °C at 200 rpm to exponential phase until OD_{600} was 0.8. The cells were diluted to an OD_{600} of 0.1. Then, 5 µl portions of tenfold dilutions of the indicated strains were spotted on SD-His with or without FK506 (1 µg ml^{-1}). After incubation at 30 °C for indicated time, plates were photographed with the 5200CE Image System (TANON). Each assay was repeated three times with similar results.

Growth curve analysis

To profile the cell growth, the WT strain and the *FKS1*-KO strain were grown in YPD media at 30 °C overnight to exponential phase. Then, cultured cells were inoculated into the fresh YPD medium with an initial OD_{600} of 0.01, which was supplemented with or without 1 µg ml^{-1} FK506. The new cultures were then grown at 30 °C till stationary phase. During the cultivation, the optical densities (OD_{600}) were measured at 8 h interval for 48 h. The experiments were done in triplicate to make the cell growth curves.

FKS1 activity assay

The yeast strains carrying different FKS1 variants with the C-terminal 3× Flag tag were generated, cultured and lysed as described above. The collected membrane was solubilized in buffer containing 50 mM Tris-HCl pH 7.4, 1 mM EDTA, 33% glycerol, 0.5% CHAPS (Anatrace), 0.1% CHS (Anatrace), 4 µM GTPγS and protease inhibitor (cOmplete protease inhibitor cocktail, Roche). FKS1 and its variants were purified using anti-Flag M2 affinity gel (Sigma) and were eluted in buffer containing 50 mM Tris-HCl pH 7.4, 1 mM EDTA, 33% glycerol, 0.2% CHAPS and 0.04% CHS, supplemented with 150 µg ml^{-1} 3× Flag peptide. The proteins purified in detergent CHAPS or GDN were assayed by using the UDP-Glo Glycosyltransferase Assay kit (Promega) to monitor the UDP released. Of FKS variants, 2.5 µl was added to 30 µl reaction mixture in total containing 50 mM Tris-HCl pH 7.4, 33% glycerol, 1 mM EDTA, 6 µg ml^{-1} Rho1, 0.2% CHAPS, 0.04% CHS, 4 µM GTPγS and 20 mM potassium fluoride (KF). The reaction was initiated by adding UDP-Glc to a final concentration of 2.5 mM. The reaction was carried out at 30 °C for 1 h. Luminescence was recorded using a Pherastar FS system (BMG Labtech). The final activity was normalized to the FKS1 amount that was measured by immunoblotting against the 3× Flag tag, using the DYKDDDDK tag monoclonal antibody (1:1,000 dilution; cat no. 66008-3-Ig, clone no. 2B3C4, Proteintech). In the case of inhibitor profiling, serial dilutions of echinocandin drugs were first incubated with FKS1 variants for 10 min at room temperature before adding other components to react.

In vitro synthesis of β-1,3-glucan and aniline blue staining

For in vitro β-1,3-glucan synthesis, the enzyme purified in detergent GDN (FKS1 or the FKS1(S643P) mutant; 0.02 mg ml^{-1}) and donor UDP-Glc (2.5 mM) were mixed in reaction buffer (50 mM Tris-HCl pH 7.4, 33% glycerol, 1 mM EDTA, 6 µg ml^{-1} Rho1, 0.2% CHAPS, 0.04% CHS, 4 µM GTPγS and 20 mM KF), in the presence or absence of 200 µM caspofungin. The reaction volume was set up as 100 µl (for aniline blue staining) or 10 ml (for product enrichment and subsequent enzymatic degradation and glycosyl linkage analysis). The reaction was carried out at 30 °C for indicated time period.

For the staining of the synthesized products by aniline blue, a 100 µl aliquot of reactants or 0.1% (w/v) of *S. cerevisiae* β-glucan (Sigma) was taken and added to equal volume of aniline blue (0.03%; Sigma). The mixture was incubated in the dark for 20 min for complete dye binding. Each sample was then loaded into a capillary and was observed under a fluorescence microscope with an excitation wavelength of 365 nm and an emission wavelength of 433 nm. Each assay was repeated three times with similar results.

Enzymatic degradation analysis of the synthesized polymer

The in vitro synthesized polymer is water-insoluble and was collected by centrifugation. It was washed twice with buffer: 50 mM Tris-HCl pH 7.4, 33% glycerol, 1 mM EDTA, 0.2% CHAPS, 0.04% CHS, 20 mM KF and twice with deionized water. Two enzymes were used for the degradation analysis of the synthesized polymer: endo-β-1,3-glucanase (*Trichoderma* sp.; product code: E-LAMSE, Megazyme) or endo-β-1,4-glucanase (*Aspergillus niger*; product code: E-CELAN, Megazyme). These two enzymes were first dialysed into the buffer (100 mM NaAc pH 4.5). Then, 0.5 U of each enzyme was added to 50 µl 1% (w/v) of synthesized polymer in 200 mM NaAc (pH 4.5). Degradation of standard controls cellulose (C6288, Sigma) or curdlan (C7821, Sigma) was also performed with the same condition[64,65]. The mixtures were incubated at 40 °C, and samples were withdrawn at various time intervals and were boiled for 5 min for reaction termination. The enzymatic degradation products were then analysed by thin-layer chromatography. In brief, a 2 µl aliquot of the withdrawn samples was spotted on a silica gel plate (Merck Silica gel 60 F254) and developed in a solvent system containing *n*-butanol:acetic acid:water (2:1:1 v/v/v). The plates were visualized by immersing in methanol:sulfuric acid (95:5 v/v) and subsequent heating at 95 °C. A mixture of glucose (G5767, Sigma), laminaribiose (O-LAM2, Megazyme), laminaritriose (O-LAM3, Megazyme) and laminarihexaose (O-LAM6, Megazyme) was used as the thin-layer chromatography standards.

During enzymatic digestion of synthesized polymer, the reducing sugars released were measured using the DNS reagents (Micro Reducing Sugar Assay Kit, Abbkine). In brief, 175 µl of the diluted hydrolysis sample was mixed with 125 µl of DNS reagent. Standard from the kit at the concentration range of 0.2–0.6 mg ml^{-1} was used for the generation of the standard curve. Reaction mixtures were boiled in a water bath for 5 min. After cooling to room temperature in a water-ice bath, the absorbance of a 0.2 ml sample was measured at 540 nm.

Glycosyl linkage (methylation) analysis

The in vitro synthesized polymer by FKS1 was washed twice with buffer: 50 mM Tris-HCl pH 7.4, 33% glycerol, 1 mM EDTA, 0.2% CHAPS, 0.04% CHS, 20 mM KF and two times with deionized water. The washed sample was then dialysed into deionized water and freeze-dried. Methylation analysis was performed following a previous study[66]. The dried sample (approximately 1 mg) was dissolved in DMSO (500 µl). The methylation was performed in DMSO/NaOH with iodomethane for 1 h. The methylated products were hydrolysed with 2 M trifluoroacetic acid at 121 °C for 90 min, reduced by NaBD4 and acetylated with acetic anhydride at 100 °C for 2.5 h. The resulting partially methylated alditol acetates were analysed using the GC-MS system (6890A-5975C, Agilent Technology) equipped with an Agilent BPX70 chromatographic column (30 m × 0.25 mm × 0.25 µm; SGE). The temperature program was set as follows: 140 °C for 2 min, 140–230 °C at 3 °C per minute and 230 °C for 3 min.

Quantitative determination of β-1,3-glucan in cell walls

The levels of β-1,3-glucan were determined using the aniline blue assay, as previously described[23,26,67–72]. Testing strains were grown in YPD media to exponential phase until OD_{600} was 0.5. The same amount of cells for each strain was collected by centrifugation at 5,000*g*. The collected cells were washed twice with TE buffer (10 mM Tris-HCl pH 8.0, and 1 mM EDTA). The pelleted cells were suspended with 0.5 ml TE buffer and mixed with 0.1 ml of 6 M NaOH. The mixture was incubated in an

80 °C water bath for 30 min to solubilize the glucan. Then, 2.1 ml of aniline blue (0.03% aniline blue, 0.18 M HCl and 0.49 M glycine-NaOH pH 9.5) was added to each sample. The samples were briefly vortexed and incubated at 50 °C for 30 min and an additional 30 min at 24 °C. Fluorescence was quantified using a fluorescence plate reader (CLARIOstar Plus, BMG Labtech) under an excitation wavelength of 400 nm and an emission wavelength of 460 nm with a cut-off of 455 nm. All samples were measured in triplicates.

Protein identification with mass spectrometry analysis

The protein samples were separated by SDS–PAGE gel and were stained with Coomassie. The gel band was manually excised and destained. The proteins were reduced with DTT, alkylated with IAA and digested with proteomics-grade trypsin in 20 mM ammonium bicarbonate[73]. The digestion was performed overnight at 37 °C and stopped by adding 2% formic acid. The peptides in gel were extracted using solution containing 2% formic acid and 67% acetonitrile. The peptides were vacuum-dried, resuspended in 0.1% formic acid, loaded onto the trap column nanoViper C18 (3 µm, 100 Å) and separated on an analytic column (Acclaim PepMap RSLC, 75 µm × 25 cm; C18 2 µm, 100 Å) using the EASY nLC 1200 HPLC system (Thermo Fisher). The elution gradient was 5–38% buffer A (0.1% formic acid and 80% acetonitrile) over 30 min. The mass spectrometry analysis was performed on a Q Exactive mass spectrometer (Thermo Fisher). The resulting data were converted to mgf file with ProteoWizard and analysed using the Mascot search engine for protein identification against a UniProt *Saccharomyces cerevisiae* database with a false discovery rate of less than 1%.

Reporting summary

Further information on research design is available in the Nature Portfolio Reporting Summary linked to this article.

Data availability

EM density maps have been deposited in the Electron Microscopy Data Bank under the accession codes EMD-33154 (FKS1) and EMD-34115 (FKS1(S643P)). The coordinates have been deposited in the PDB under the accession codes 7XE4 (FKS1) and 7YUY (FKS1(S643P)). This study analysed several protein structures publicly available from the PDB under the accession codes 4HG6, 6WLB, 7SP7, 6YV8, 6iwr, 6h4m and 1qgq.

48. Funakoshi, M. & Hochstrasser, M. Small epitope-linker modules for PCR-based C-terminal tagging in *Saccharomyces cerevisiae*. *Yeast* **26**, 185–192 (2009).
49. Toulmay, A. & Schneiter, R. A two-step method for the introduction of single or multiple defined point mutations into the genome of *Saccharomyces cerevisiae*. *Yeast* **23**, 825–831 (2006).
50. Zheng, S. Q. et al. MotionCor2: anisotropic correction of beam-induced motion for improved cryo-electron microscopy. *Nat. Methods* **14**, 331–332 (2017).
51. Rohou, A. & Grigorieff, N. CTFFIND4: fast and accurate defocus estimation from electron micrographs. *J. Struct. Biol.* **192**, 216–221 (2015).
52. Zivanov, J. et al. New tools for automated high-resolution cryo-EM structure determination in RELION-3. *eLife* **7**, e42166 (2018).
53. Rosenthal, P. B. & Henderson, R. Optimal determination of particle orientation, absolute hand, and contrast loss in single-particle electron cryomicroscopy. *J. Mol. Biol.* **333**, 721–745 (2003).
54. Kucukelbir, A., Sigworth, F. J. & Tagare, H. D. Quantifying the local resolution of cryo-EM density maps. *Nat. Methods* **11**, 63–65 (2014).
55. Adams, P. D. et al. PHENIX: a comprehensive Python-based system for macromolecular structure solution. *Acta Crystallogr. D Biol. Crystallogr.* **66**, 213–221 (2010).
56. Emsley, P., Lohkamp, B., Scott, W. G. & Cowtan, K. Features and development of Coot. *Acta Crystallogr. D Biol. Crystallogr.* **66**, 486–501 (2010).
57. Chen, V. B. et al. MolProbity: all-atom structure validation for macromolecular crystallography. *Acta Crystallogr. D Biol. Crystallogr.* **66**, 12–21 (2010).
58. Afonine, P. V. et al. New tools for the analysis and validation of cryo-EM maps and atomic models. *Acta Crystallogr. D Struct. Biol.* **74**, 814–840 (2018).
59. Holm, L. & Laakso, L. M. Dali server update. *Nucleic Acids Res.* **44**, W351–W355 (2016).
60. Jumper, J. et al. Highly accurate protein structure prediction with AlphaFold. *Nature* **596**, 583–589 (2021).
61. Varadi, M. et al. AlphaFold Protein Structure Database: massively expanding the structural coverage of protein-sequence space with high-accuracy models. *Nucleic Acids Res.* **50**, D439–D444 (2022).
62. Pettersen, E. F. et al. UCSF Chimera—a visualization system for exploratory research and analysis. *J. Comput. Chem.* **25**, 1605–1612 (2004).
63. Pettersen, E. F. et al. UCSF ChimeraX: structure visualization for researchers, educators, and developers. *Protein Sci.* **30**, 70–82 (2021).
64. Zhang, Y. H., Cui, J., Lynd, L. R. & Kuang, L. R. A transition from cellulose swelling to cellulose dissolution by o-phosphoric acid: evidence from enzymatic hydrolysis and supramolecular structure. *Biomacromolecules* **7**, 644–648 (2006).
65. McIntosh, M., Stone, B. A. & Stanisich, V. A. Curdlan and other bacterial (1→3)-β-D-glucans. *Appl. Microbiol. Biot.* **68**, 163–173 (2005).
66. Ciucanu, I. & Kerek, F. A simple and rapid method for the permethylation of carbohydrates. *Carbohydr. Res.* **131**, 209–217 (1984).
67. Shedletzky, E., Unger, C. & Delmer, D. P. A microtiter-based fluorescence assay for (1,3)-β-glucan synthases. *Anal. Biochem.* **249**, 88–93 (1997).
68. Kahn, J. N., Hsu, M. J., Racine, F., Giacobbe, R. & Motyl, M. Caspofungin susceptibility in *Aspergillus* and non-*Aspergillus* molds: inhibition of glucan synthase and reduction of β-D-1,3 glucan levels in culture. *Antimicrob. Agents Chemother.* **50**, 2214–2216 (2006).
69. Sekiya-Kawasaki, M. et al. Dissection of upstream regulatory components of the Rho1p effector, 1,3-β-glucan synthase, in *Saccharomyces cerevisiae*. *Genetics* **162**, 663–676 (2002).
70. Watanabe, D., Abe, M. & Ohya, Y. Yeast Lrg1p acts as a specialized RhoGAP regulating 1,3-β-glucan synthesis. *Yeast* **18**, 943–951 (2001).
71. Lee, K. K. et al. Yeast species-specific, differential inhibition of β-1,3-glucan synthesis by poacic acid and caspofungin. *Cell Surf.* **3**, 12–25 (2018).
72. Anjos, J. et al. β(1,3)-Glucan synthase complex from *Alternaria infectoria*, a rare dematiaceous human pathogen. *Med. Mycol.* **50**, 716–725 (2012).
73. Shevchenko, A., Tomas, H., Havlis, J., Olsen, J. V. & Mann, M. In-gel digestion for mass spectrometric characterization of proteins and proteomes. *Nat. Protoc.* **1**, 2856–2860 (2006).

Acknowledgements We thank all staff members at the Cryo-EM Center, Southern University of Science and Technology for their assistance in data collection; and J. Zhao for advice on thin-layer chromatography. This work was supported by the National Natural Science Foundation of China (92053112 and 31971148 to H.Y., 32100575 to Min Zhang and 82188101 to Mingjie Zhang), ShenZhen Talent Program KQTD20210811090115021 (to Mingjie Zhang and X.L.), the Fundamental Research Funds for the Central Universities (5003510056 to H.Y. and 5003510112 to Min Zhang) and Program of HUST Academic Frontier Youth Team (2018QYTD02 to H.Y.).

Author contributions X.H., P.Y., Min Zhang, X.L. and H.Y. prepared the sample, collected the data and solved the structures. X.H., P.Y. and Min Zhang performed the functional experiments, assisted by C.C., J.L., H.S. and Y.W. Mingjie Zhang, Min Zhang, X.L. and H.Y. designed the experiments, analysed the data and wrote the manuscript.

Competing interests The authors declare no competing interests.

Additional information

Supplementary information The online version contains supplementary material available at https://doi.org/10.1038/s41586-023-05856-5.

Correspondence and requests for materials should be addressed to Min Zhang, Xiaotian Liu or Hongjun Yu.

Peer review information *Nature* thanks Vincent Bulone and the other, anonymous, reviewer(s) for their contribution to the peer review of this work.

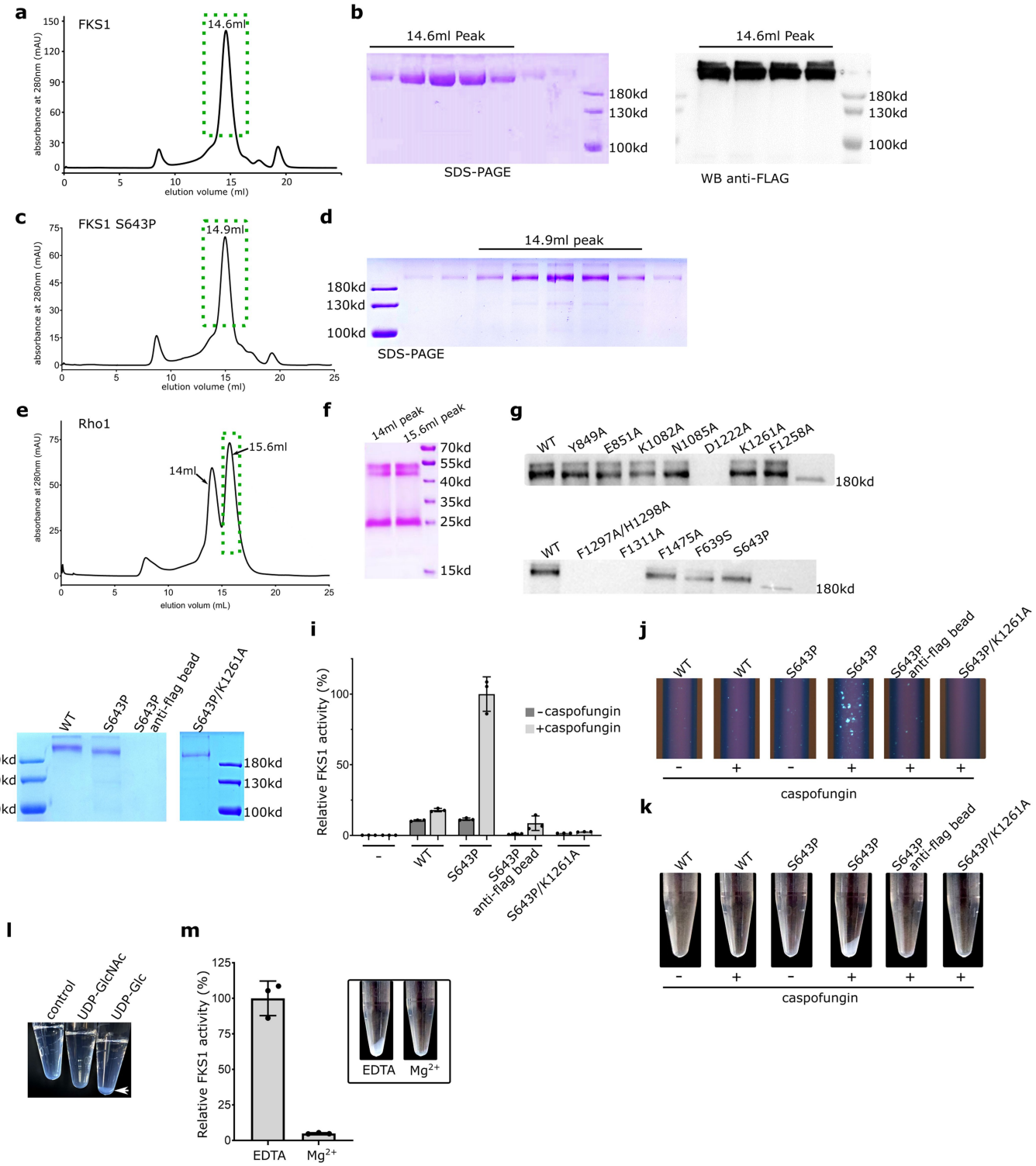

Extended Data Fig. 1 | See next page for caption.

Extended Data Fig. 1 | Sample preparation, functional characterization and in vitro product synthesis. a, Elution profile of Gel-filtration chromatography (Superose 6 Increase 10/300 GL) of FKS1 purified in detergent GDN. Green dashed box marks the fractions pooled for cryoEM analysis. **b**, SDS-PAGE (left) and western blot (right) analysis of the fractions of the monodisperse elution peak in (**a**). Representative gel and western-blot image among 3 replicates are shown. **c**, Elution profile of Gel-filtration chromatography (Superose 6 Increase 10/300 GL) of FKS1 S643 purified in detergent GDN. Green dashed box marks the fractions pooled for cryoEM analysis and product synthesis. **d**, SDS-PAGE analysis of the fractions of the monodisperse elution peak in (**c**). A representative gel among 3 replicates is shown. **e**, Elution profile of Gel-filtration chromatography (Superdex 200 Increase 10/300 GL) of Rho1. Green dashed box marks the fractions pooled for activity assay and product synthesis. **f**, SDS-PAGE analysis of the fractions of the monodisperse elution peak in (**e**). Two peaks in (**e**) shows similar three-band pattern (**f**), and all three bands were identified as Rho1 by Mass Spec analysis. A representative gel among 3 replicates is shown. **g**, Western blot analyses of wild-type FKS1 and different FKS1 variants purified in detergent CHAPS. A representative image among 3 replicates is shown. **h**, SDS-PAGE analysis of GDN-purified flag-tagged FKS1 variants, which were used for the assays of activity (**i**-**j**) and product synthesis (**k**). First lane, FKS1 WT; second lane, FKS1 S643P (the echinocandin-resistant mutant); third lane, purified FKS1 S643P is immunodepleted by anti-flag beads; fourth lane, FKS1 S643P/K1261A. A representative gel among 3 replicates is shown. For (**b**,**d**,**f**,**g**,**h**), their full scans are provided in Supplementary Fig. 1. **i**, In vitro activity of FKS1 variants purified in GDN. The activity was assayed by monitoring UDP generated (1-h reaction). Data are mean ± SEM, n = 3 independent experiments. **j**–**k**, In vitro product synthesis assay by FKS1 variants purified in GDN. The assay was performed either by staining the synthesized products with dye aniline blue (**j**; 12-h reaction) or by visualization of the products synthesized (**k**; 48-h reaction). These experiments were repeated three times with similar results. **l**, Donor specificity of product synthesis by GDN-purified FKS1 S643P. Water-insoluble polymers (indicated by white arrow) appear only in the presence of UDP-Glc instead of UDP-GlcNAc. This experiment was repeated three times with similar results. **m**, The effects of Mg^{2+} on the catalytic activity of GDN-purified FKS1 S643P. Activity was assayed in the presence of 1 mM EDTA or 200 μM Mg^{2+}. Data are mean ± SEM, n = 3 independent experiments. Inset, product synthesis in the presence of 1 mM EDTA or 200 μM Mg^{2+}. This experiment was repeated three times with similar results.

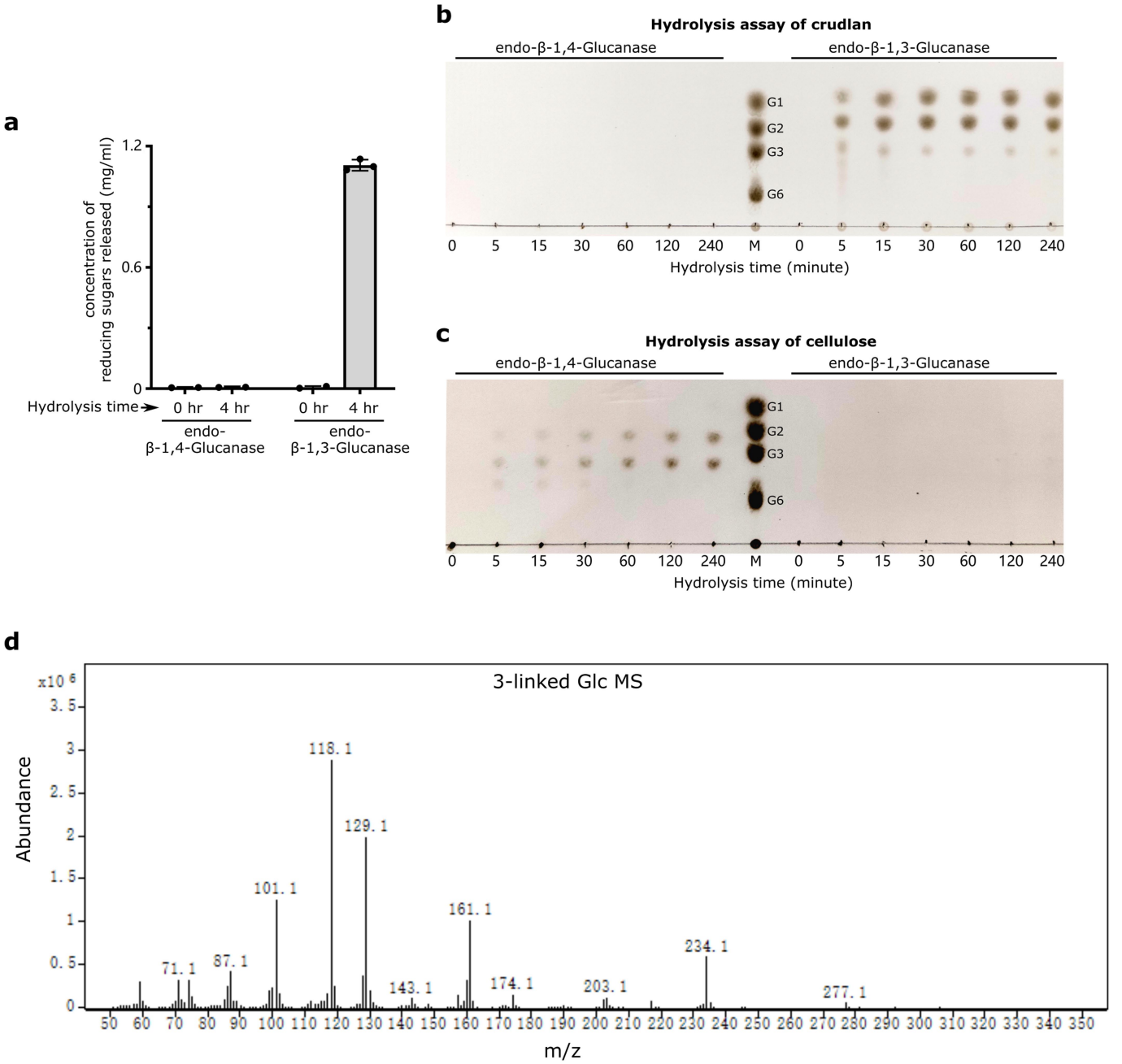

Extended Data Fig. 2 | Enzymatic hydrolysis and glycosyl linkage (methylation) analysis of FKS1-synthesized products. a, Quantification of the released reducing sugars during enzymatic digestion of the water-insoluble polymer synthesized by GDN-purified FKS1 S643P. Two specific glucanases were used: specific endo-1,3-β-glucanase and endo-1,4-β-glucanase. Data are mean ± SEM, n = 3 independent experiments. **b**–**c**, The hydrolysis specificity of endo-1,3-β-Glucanase and endo-1,4-β-Glucanase was tested against standard polysaccharide β-1,3-glucan curdlan (**b**) and cellulose (**c**). A mixture of glucose (G1), laminaribiose (G2), laminaritriose (G3) and laminarihexaose (G6) was used as the standards (lane M). **d**, Mass spectrum of GC peak (11.64min) in (Fig. 1f) reveals the identity of this PMAA as 1,3,5-tri-O-acetyl-2,4,6-tri-O-methyl glucitol, confirming 1,3-Glc*p* linkage.

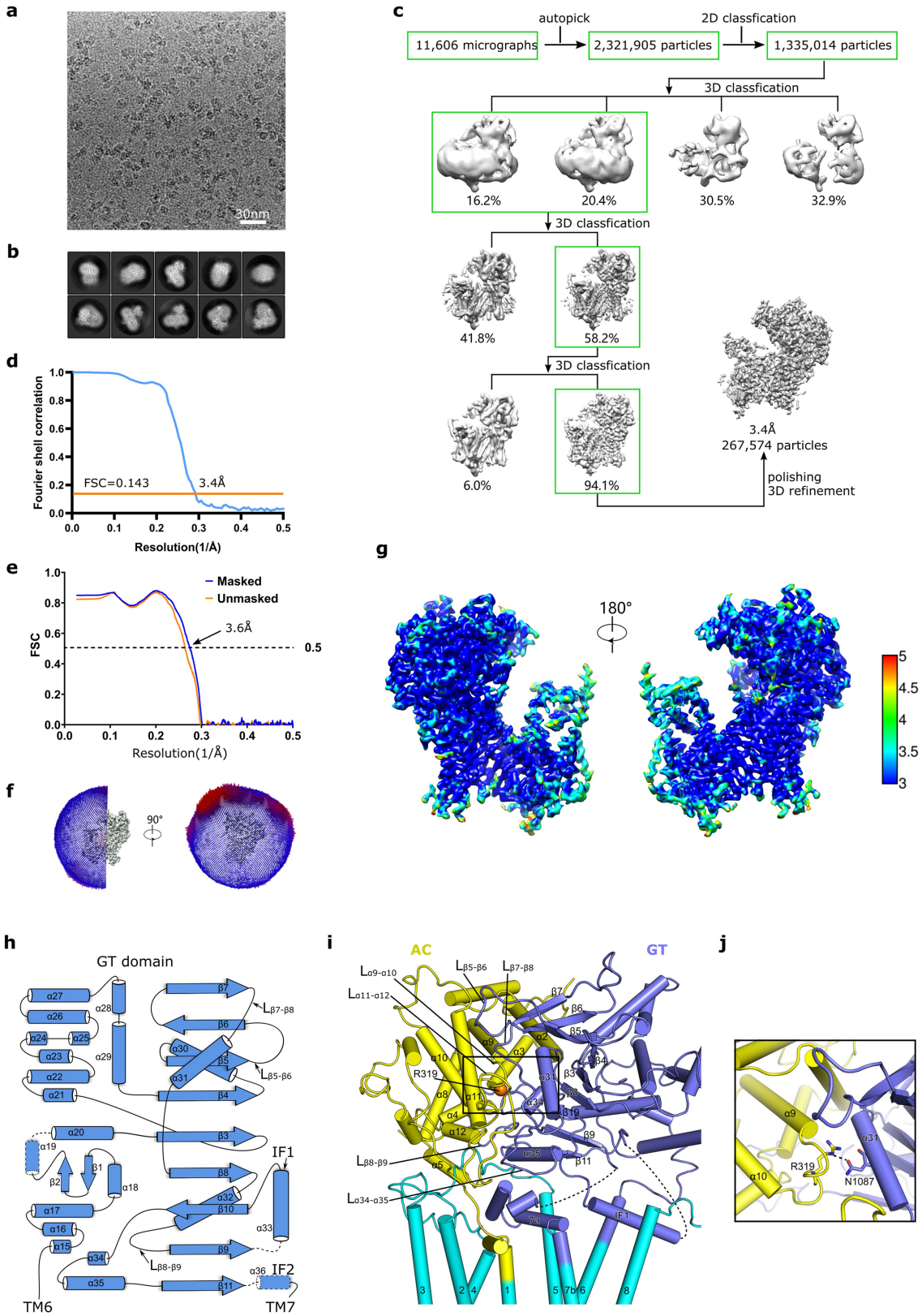

Extended Data Fig. 3 | See next page for caption.

Extended Data Fig. 3 | Cryo-EM structural determination of *S. cerevisiae* FKS1 and structural features of FKS1 cytoplasmic region. **a**, A representative cryo-EM micrograph of FKS1 from 11606 collected micrographs. **b**, Representative 2D class averages. **c**, Flow chart of cryo-EM data acquisition and data processing of FKS1. See Methods for more details. **d**, The gold-standard Fourier shell correlation (FSC) curve of the reconstructed map. **e**, The FSC curve between model and map, which is calculated by PHENIX.mtriage[58]. **f**, Cutaway views of the angular distribution of all particles used in the final 3D reconstruction. **g**, Local resolution distribution of the final cryo-EM map of FKS1, calculated with ResMap[54]. **h**, Topological diagram of FKS1 GT-domain. Flexible segments invisible in the 3D reconstruction are depicted by dashed lines. **i**, Interactions between AC and GT domain. Labeled are central β strands and the structural elements involved in the extensive contacting interface: α2-5, α8-11, loops Lα9-α10 and Lα11-α12 of AC domain; α31, α34-35, loops Lβ5-β6, Lβ7-β8; Lβ8-β9 of GT domain). The FKS1 R319, a previously identified essential residue for FKS1[24], is marked by its Cα atom as sphere and is embedded in this interface. **j**, Zoomed in view of the boxed region in (**i**), showing the interaction between R319 and N1087 to maintain the interface between AC and GT domain.

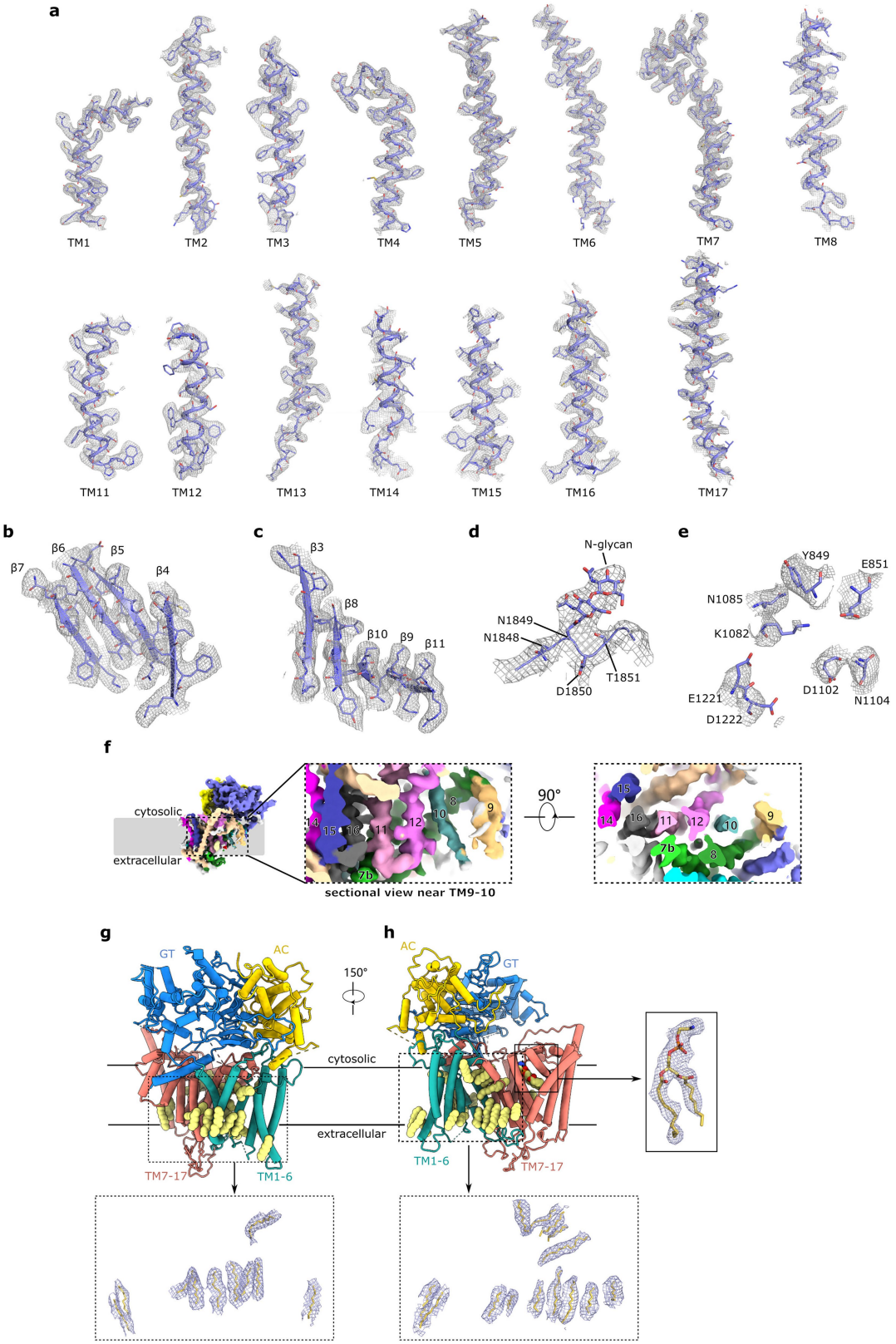

Extended Data Fig. 4 | Fit of cryo-EM map with FKS1 model in example regions. a, Cryo-EM densities of TM1-8, 11–17. **b**-**c**, Cryo-EM densities of the continuous central β-sheet of 9 strands featured in FKS1 GT domain. **d**, Cryo-EM density of the N-glycan on N1849. **e**, Cryo-EM densities of active site. **f**, Cutaway view of the cryo-EM densities near TM9 and TM10. The map is segmented and colored as in Fig. 2a. The densities corresponding to TM helices TM7-12, TM14-16 are denoted by numbers. Only TM9-10 main chain can be traced from this map, though they exhibit weaker densities than other TM helices. **g**–**h**, Two views of FKS1 model with bound lipids. FKS1 model is colored as Fig. 1h and ordered lipids are shown as yellow spheres. The cryo-EM densities of the lipids are illustrated in the dashed boxes. The position and the density of the phospholipid embedded within the transmembrane domain is shown in the solid box.

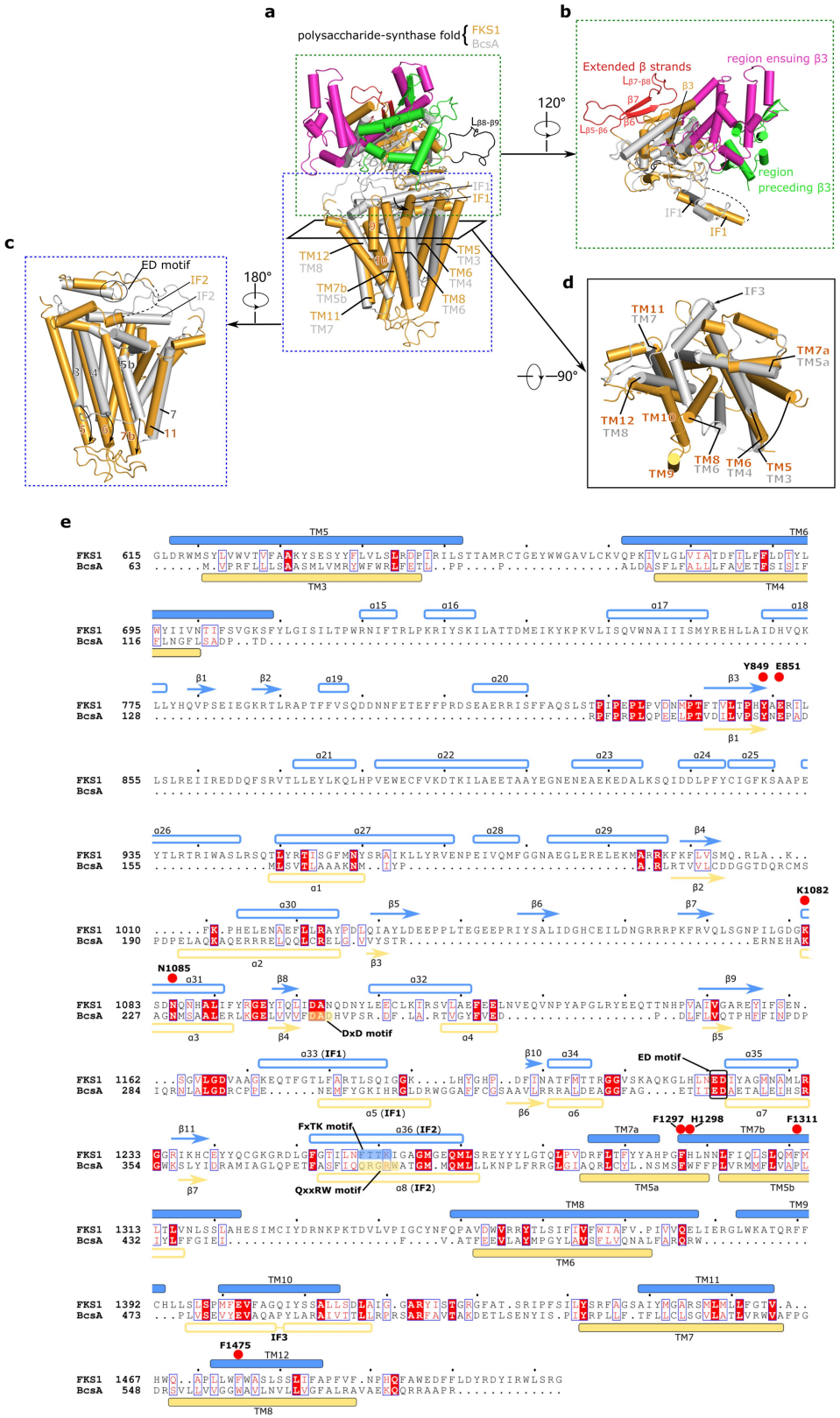

Extended Data Fig. 5 | See next page for caption.

Extended Data Fig. 5 | Structure and sequence comparison of the conserved cellulose-synthase-like folds between FKS1 and BcsA. a, The conserved fold of FKS1 (residues 615–1510) was superposed with that of BcsA (PDB ID: 4P00; residues 63–584), with an RMSD value of 4.3 Å over 308 aligned residues. BcsA is colored in grey. FKS1 core is colored in orange while FKS1-exclusive elements in its GT domain are in color-coded display as labeled in (**a**) and (**b**). Corresponding TM helices are denoted as labels while TM9 and TM10 are exclusive for FKS1. **b**, Close-up view of the superimposed GT domains in (**a**). The central β-sheet featured in GT domain gains extension in FKS1. The extended stands β6 and β7 in FKS1 and the elongated loop Lβ8-β9 contribute to a substantial portion of the interacting interface with AC domain in FKS1 (Fig. 1j). Moreover, two FKS1-specific sub-regions inserts to two sides of β3, the first strand of central β-sheet. The sub-region preceding β3 (residues 719–840) contains six helices and a pair of antiparallel β-strands (β1, β2); the sub-region ensuing β3 (residues 848–998) is α-helical, composed of 9 helices. These two sub-regions interact to pack the central β-sheet from one side. **c**, Back view of the superimposed transmembrane domains. **d**, Close-up view of superimposed membrane-cytosol interfaces. Interface helix IF1 is preserved in FKS1, which shows dramatic rearrangement relative to that of BcsA. Interface helix IF2 connecting a beta-sheet and transmembrane domain is preserved in FKS1 but disordered in the structure, which is also indicated in (**c**). Interface helix IF3 is gone in FKS1 and it is replaced by transmembrane helices TM9 and TM10 in FKS1. **e**, Structure-based sequence alignment of the conserved cellulose-synthase-like folds between FKS1 and BcsA. The alignment was first generated using PROMALS3D and then illustrated using ESPript3 server. Residues and motifs with important functions are labeled. Shown above and below the alignment are secondary structural elements derived FKS1 structure (blue symbol) and BcsA structure (PDB ID: 4P00) (orange symbol), respectively. The symbols are TM helices (filled bar), helices (empty bar) and β strands (arrow).

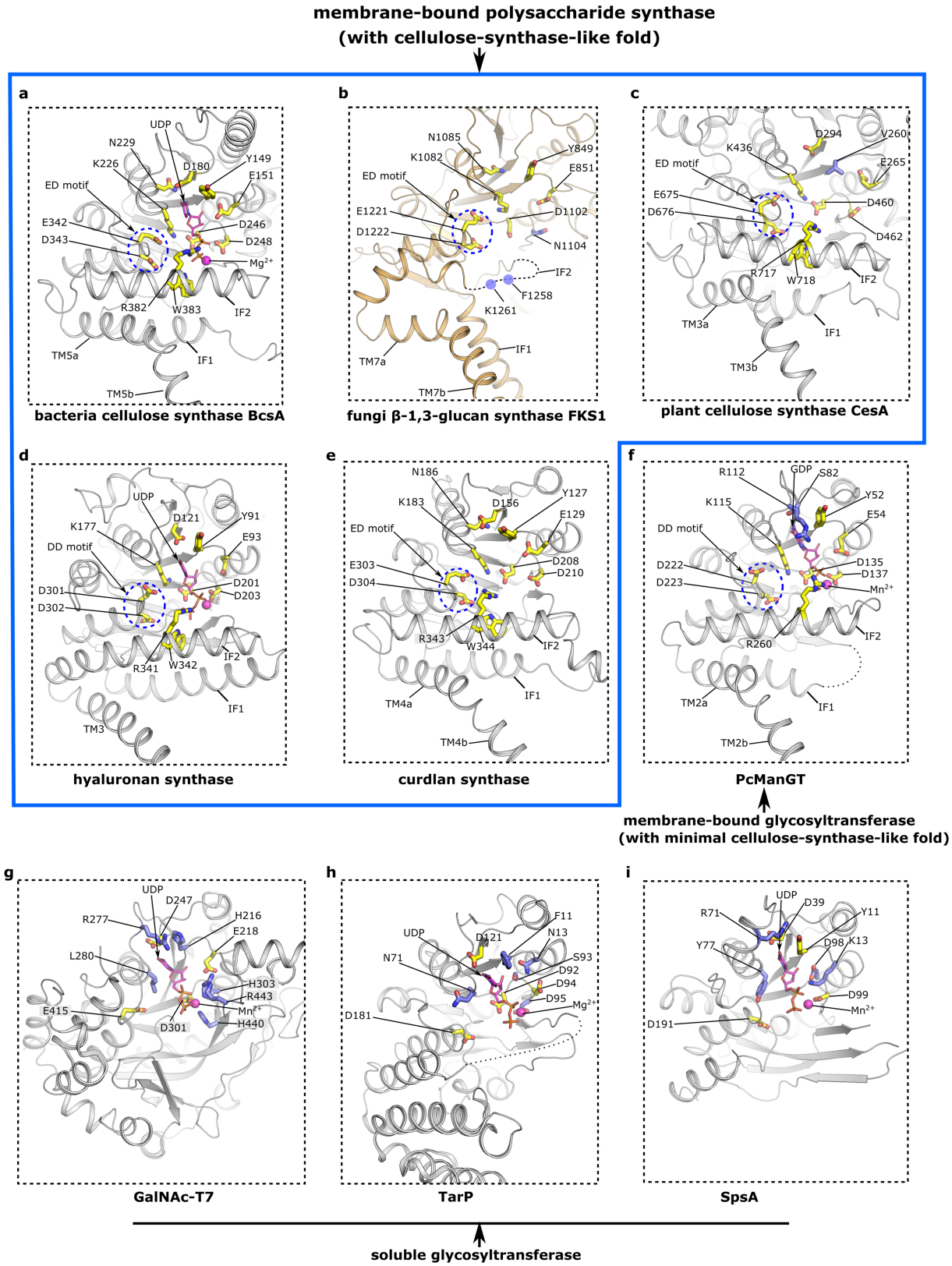

Extended Data Fig. 6 | See next page for caption.

Extended Data Fig. 6 | Overlay of the GT catalytic domains of the structural matches to FKS1 by DALI analysis. The analyzed GT catalytic domains are overlaid and shown separately as cartoon. Residues involved in substrate binding or catalysis are indicated as sticks. The bound nucleotide is shown as thin magenta sticks. The conserved residues are highlighted as yellow when using the active site of bacterial cellulose synthase BcsA (**a**) as reference. **a**–**f**, Overlay of GT catalytic domains of membrane-bound glycosyltransferases: bacterial cellulose synthase BcsA (**a**; PDB ID: 4hg6), β-1,3-glucan synthase FKS1 (**b**), plant cellulose synthase CesA (**c**; PDB ID: 6wlb), virus hyaluronan synthase (**d**; PDB ID: 7sp7), Agrobacterium curdlan synthase (**e**; model from AlphaFold Database; Uniprot ID: Q9X2V0), archaeal mannosyltransferase PcManGT (**f**; PDB ID: 6YV8). The panels outlined by blue box (**a**–**e**) are membrane-bound polysaccharide synthases containing cellulose-synthase-like fold as shown in Fig. 2f–m. PcManGT (panel **f**) contains half membrane tunnel of BcsA, and it was proposed to have a minimal cellulose-synthase-like fold[35]. **g**–**i**, Overlay of GT catalytic domains of soluble glycosyltransferases: human GalNAc-T7 (**g**; PDB ID: 6iwr), *S. aureus* TarP (**h**; PDB ID:6h4m), *B. subtilis* SpsA (**i**; PDB ID: 1qgq).

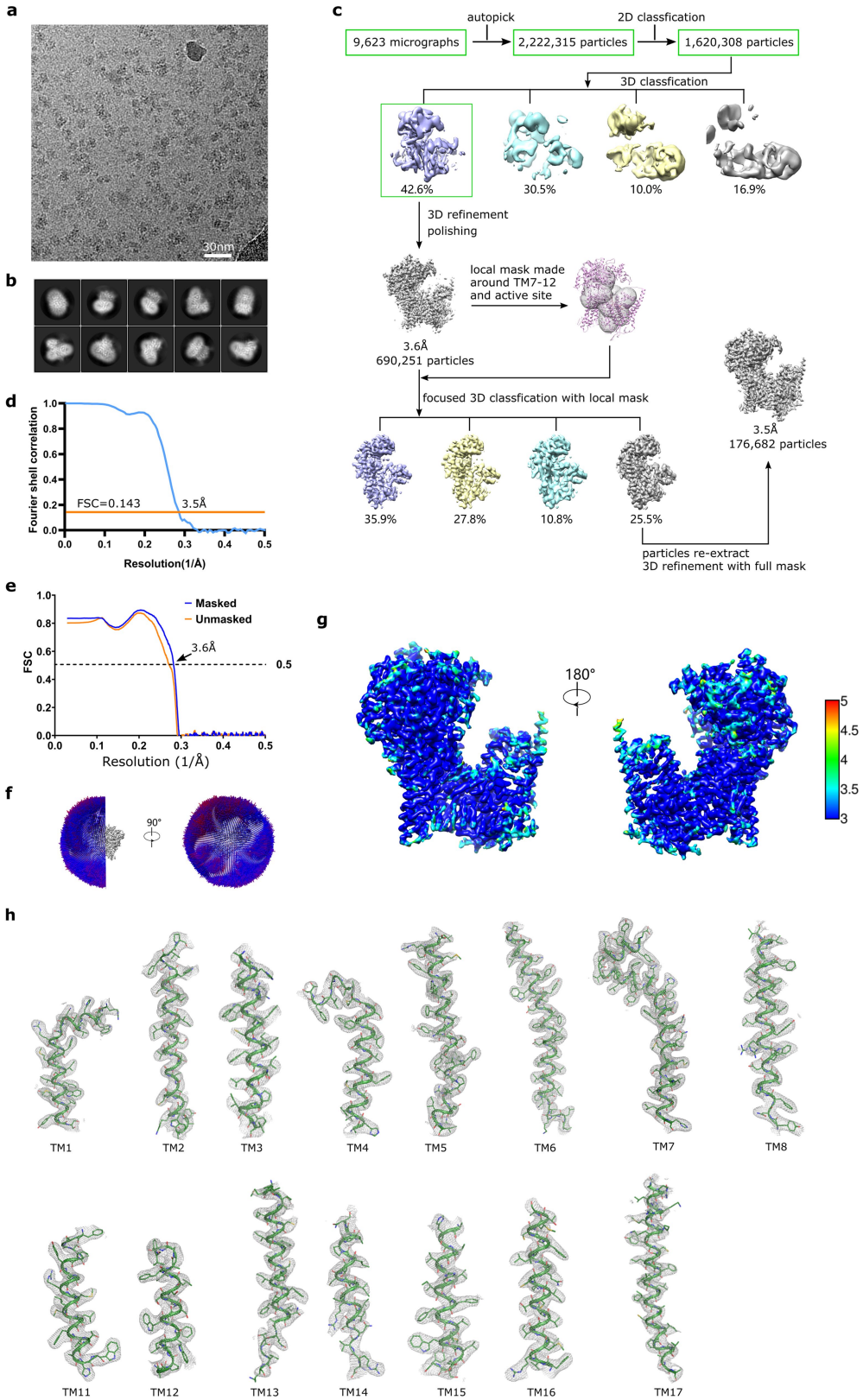

Extended Data Fig. 7 | Cryo-EM analysis of FKS1 S643P, a drug-resistant mutant of the enzyme. a, A representative cryo-EM micrograph of FKS1 S643P from 9623 collected micrographs. **b**, Representative 2D class averages. **c**, Flow chart of cryo-EM data acquisition and data processing of FKS1 S643P. See Methods for more details. **d**, The gold-standard Fourier shell correlation (FSC) curve of the reconstructed map. **e**, The FSC curve between model and map, which is calculated by PHENIX.mtriage[58]. **f**, Cutaway views of the angular distribution of all particles used in the final 3D reconstruction. **g**, Local resolution distribution of the final cryo-EM map of FKS1 S643P, calculated with ResMap. **h**, Fit of cryo-EM map with FKS1 S643P model in example regions.

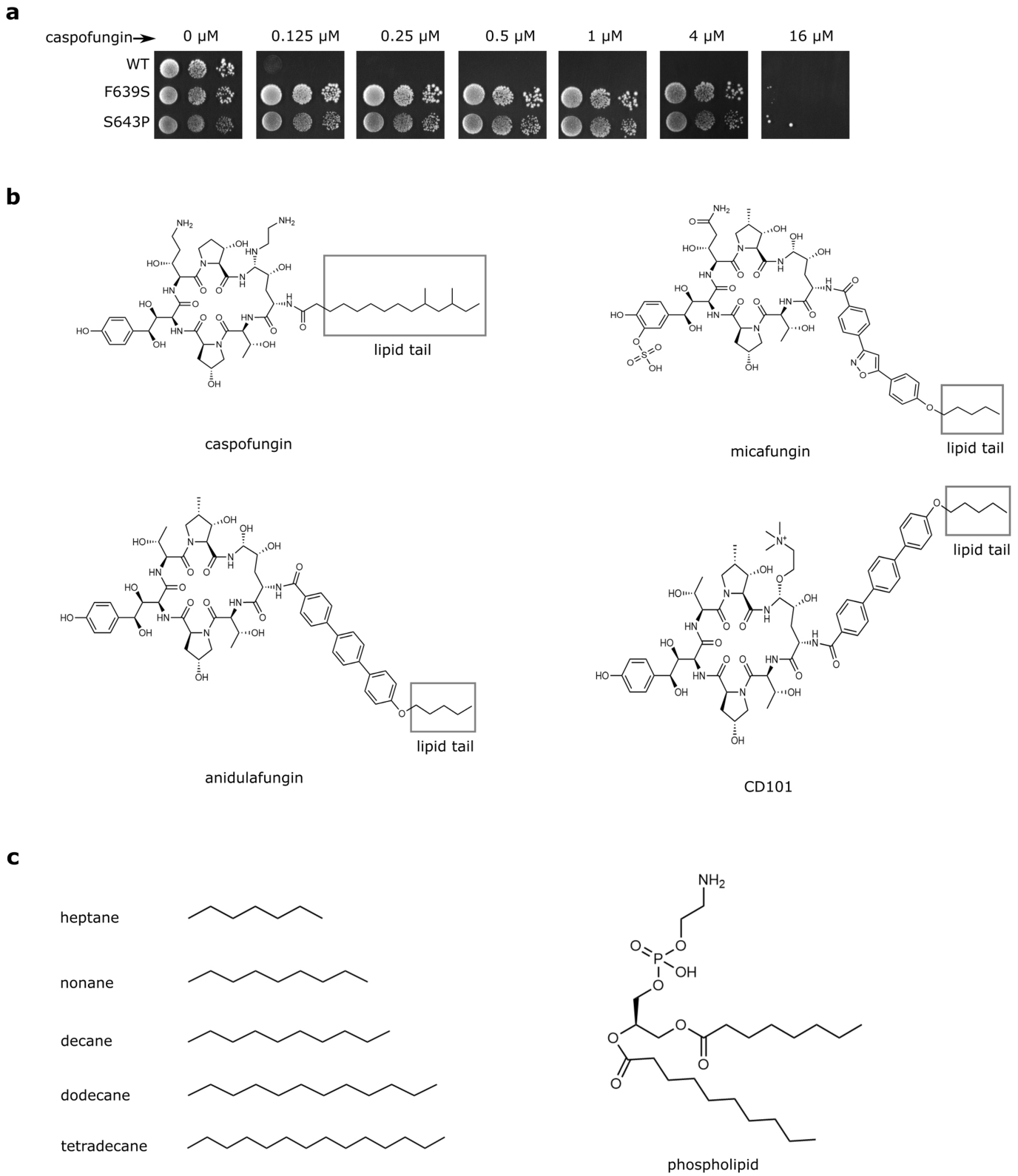

Extended Data Fig. 8 | Analysis of caspofungin-resistant phenotype and chemical structure of echinocandin drugs. a, Analysis of caspofungin-resistant phenotype of *S. cerevisiae* strain with indicated FKS1 mutations. The concentrations of caspofungin tested are indicated on the top. **b**, Chemical structure of four types of echinocandin drugs. They all feature a lipid tail as highlighted by the box. **c**, Chemical structure of the lipid alkyl chains (left panel) and phospholipid (right panel) identified from FKS1 structure.

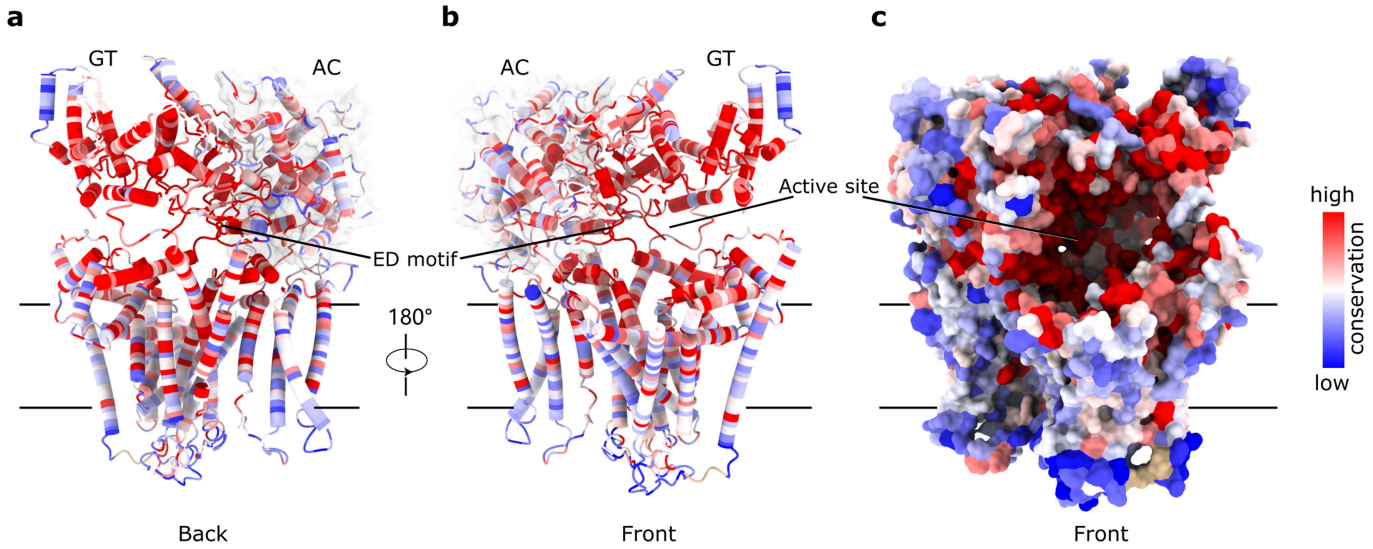

Extended Data Fig. 9 | Sequence conservation of fungi FKS illustrated on *S. cerevisiae* FKS1 structure. a–**c**, FKS1 structure is colored according to level of sequence conservation (red, high; blue, low). **a**–**b**, Back and front view parallel to the membrane, in cartoon display. **c**, The same view as (**b**) with surface representation.

Extended Data Table 1 | Cryo-EM data collection, refinement and validation statistics

	FKS1 (EMDB-33154) (PDB 7XE4)	FKS1 S643P (EMDB-34115) (PDB 7YUY)
Data collection and processing		
Magnification	130,000	130,000
Voltage (kV)	300	300
Electron exposure (e–/Å^2)	50	50
Defocus range (μm)	-1.2 to -3	-1.2 to -3
Pixel size (Å)	0.92	0.92
Symmetry imposed	C1	C1
Initial particle images (no.)	2,321,905	2,222,315
Final particle images (no.)	267,574	176,682
Map resolution (Å)	3.4	3.5
FSC threshold	0.143	0.143
Map resolution range (Å)*	3.0-6.0	3.0-6.0
Refinement		
Initial model used (PDB code)	n/a	7XE4
Model resolution (Å)	3.6	3.6
FSC threshold	0.5	0.5
Model resolution range (Å)*	3.0-6.0	3.0-6.0
Map sharpening *B* factor (Å^2)	-53.6	-108.5
Model composition		
Non-hydrogen atoms	12246	12291
Protein residues	1503	1503
Ligands	25 lipids; 1 N-glycan	25 lipids; 1 N-glycan; 1 laminaritetraose
B factors (Å^2)		
Protein	124	83
Ligand	100	59
R.m.s. deviations		
Bond lengths (Å)	0.005	0.005
Bond angles (°)	0.856	0.836
Validation		
MolProbity score	2.0	2.0
Clashscore	8.2	7.3
Poor rotamers (%)	0.8	0.3
Ramachandran plot		
Favored (%)	89.6	90.1
Allowed (%)	10.0	9.7
Disallowed (%)	0.4	0.2

*Local resolution range

nature portfolio

Corresponding author(s): Hongjun Yu

Last updated by author(s): Jan 18, 2023

Reporting Summary

Nature Portfolio wishes to improve the reproducibility of the work that we publish. This form provides structure for consistency and transparency in reporting. For further information on Nature Portfolio policies, see our Editorial Policies and the Editorial Policy Checklist.

Statistics

For all statistical analyses, confirm that the following items are present in the figure legend, table legend, main text, or Methods section.

n/a	Confirmed	
☐	☒	The exact sample size (*n*) for each experimental group/condition, given as a discrete number and unit of measurement
☐	☒	A statement on whether measurements were taken from distinct samples or whether the same sample was measured repeatedly
☒	☐	The statistical test(s) used AND whether they are one- or two-sided *Only common tests should be described solely by name; describe more complex techniques in the Methods section.*
☒	☐	A description of all covariates tested
☒	☐	A description of any assumptions or corrections, such as tests of normality and adjustment for multiple comparisons
☐	☒	A full description of the statistical parameters including central tendency (e.g. means) or other basic estimates (e.g. regression coefficient) AND variation (e.g. standard deviation) or associated estimates of uncertainty (e.g. confidence intervals)
☒	☐	For null hypothesis testing, the test statistic (e.g. *F*, *t*, *r*) with confidence intervals, effect sizes, degrees of freedom and *P* value noted *Give P values as exact values whenever suitable.*
☒	☐	For Bayesian analysis, information on the choice of priors and Markov chain Monte Carlo settings
☒	☐	For hierarchical and complex designs, identification of the appropriate level for tests and full reporting of outcomes
☒	☐	Estimates of effect sizes (e.g. Cohen's *d*, Pearson's *r*), indicating how they were calculated

Our web collection on statistics for biologists contains articles on many of the points above.

Software and code

Policy information about availability of computer code

Data collection	FEI EPU 2.7; SerialEM 3.8;
Data analysis	MotionCor2 1.1.0; CTFFIND4 4.1.5; RELION 3.0; Chimera 1.15; ChimeraX 1.1; Coot 0.8.9; Phenix 1.19; Pymol 2.4; DALI server; AlphaFold database;

For manuscripts utilizing custom algorithms or software that are central to the research but not yet described in published literature, software must be made available to editors and reviewers. We strongly encourage code deposition in a community repository (e.g. GitHub). See the Nature Portfolio guidelines for submitting code & software for further information.

Data

Policy information about availability of data

All manuscripts must include a data availability statement. This statement should provide the following information, where applicable:

- Accession codes, unique identifiers, or web links for publicly available datasets
- A description of any restrictions on data availability
- For clinical datasets or third party data, please ensure that the statement adheres to our policy

EM density maps have been deposited in Electron Microscopy Data Bank under accession codes EMD-33154 (FKS1), EMD-34115 (FKS1 S643P). The coordinates have been deposited in Protein Data Bank under accession codes 7XE4 (FKS1), 7YUY (FKS1 S643P). This study analyzed several protein structures publicly available from Protein Data Bank under accession codes 4hg6, 6wlb, 7sp7, 6yv8, 6iwr, 6h4m and 1qgq.

Field-specific reporting

Please select the one below that is the best fit for your research. If you are not sure, read the appropriate sections before making your selection.

☒ Life sciences ☐ Behavioural & social sciences ☐ Ecological, evolutionary & environmental sciences

For a reference copy of the document with all sections, see nature.com/documents/nr-reporting-summary-flat.pdf

Life sciences study design

All studies must disclose on these points even when the disclosure is negative.

Sample size	No statistical methods were used to predetermine sample size. Experiments were typically repeated in triplicates to ensure reproducibility. Sufficient amount of cryoEM data was collected to achieve fine quality of the resulting cryoEM map, indicating sufficient sample size of cryoEM data.
Data exclusions	No data were excluded from the analyses.
Replication	Each experiment was repeated at least three times in independent experiments. All attempts at replication were successful.
Randomization	Randomization is not relevant as group allocation was not performed in this study and this study does not include experiments that require randomization.
Blinding	This is not applicable as this study does not include experiments that requires blinding.

Reporting for specific materials, systems and methods

We require information from authors about some types of materials, experimental systems and methods used in many studies. Here, indicate whether each material, system or method listed is relevant to your study. If you are not sure if a list item applies to your research, read the appropriate section before selecting a response.

Materials & experimental systems

n/a	Involved in the study
☐	☒ Antibodies
☐	☒ Eukaryotic cell lines
☒	☐ Palaeontology and archaeology
☒	☐ Animals and other organisms
☒	☐ Human research participants
☒	☐ Clinical data
☒	☐ Dual use research of concern

Methods

n/a	Involved in the study
☒	☐ ChIP-seq
☒	☐ Flow cytometry
☒	☐ MRI-based neuroimaging

Antibodies

Antibodies used	commercial DYKDDDDK tag Monoclonal antibody (proteintech, cat no:66008-3-Ig; clone no: 2B3C4)
Validation	The validation of this commercial antibody can be found at the website: https://www.ptglab.com/products/Flag-tag-Antibody-66008-3-Ig.htm

Eukaryotic cell lines

Policy information about cell lines

Cell line source(s)	Saccharomyces cerevisiae BY4742 (ATCC)
Authentication	No further authentications were performed for this study.
Mycoplasma contamination	No mycoplasma contamination test was tested for this study.
Commonly misidentified lines (See ICLAC register)	n/a